Diffusion-weighted and PET/MR Imaging after Radiation Therapy for Malignant Head and Neck Tumors[1]

Arthur Varoquaux, MD
Olivier Rager, MD
Pavel Dulguerov, MD
Karim Burkhardt, MD
Angeliki Ailianou, MD
Minerva Becker, MD

Abbreviations: ADC = apparent diffusion coefficient, CECT = contrast-enhanced CT, DW = diffusion-weighted, FDG = fluorine 18 fluorodeoxyglucose, IMRT = intensity-modulated radiation therapy, SCC = squamous cell carcinoma, STIR = short inversion time inversion-recovery, SUV = standardized uptake value

RadioGraphics 2015; 35:1502–1527

Published online 10.1148/rg.2015140029

Content Codes: HN MR NM NR OI

[1]From the Department of Imaging, Divisions of Radiology (A.V., A.A., M.B.) and Nuclear Medicine (O.R.); Department of Clinical Neurosciences, Division of Otorhinolaryngology–Head and Neck Surgery (P.D.); and Department of Medical Genetics and Laboratory, Division of Clinical Pathology (K.B.); Geneva University Hospital, University of Geneva, Rue Gabrielle Perret Gentil 4, 1211 Geneva 14, Switzerland. Recipient of a Magna Cum Laude award for an education exhibit at the 2013 RSNA Annual Meeting. Received February 9, 2014; revision requested May 23 and received October 4; accepted October 6. For this journal-based SA-CME activity, the authors, editor, and reviewers have disclosed no relevant relationships. **Address correspondence to** M.B. (e-mail: *Minerva.Becker@hcuge.ch*).

Supported by the Swiss National Science Foundation (grant no. SNF 320030_135728/1).

Interpreting imaging studies of the irradiated neck constitutes a challenge because of radiation therapy–induced tissue alterations, the variable appearances of recurrent tumors, and functional and metabolic phenomena that mimic disease. Therefore, morphologic magnetic resonance (MR) imaging, diffusion-weighted (DW) imaging, positron emission tomography with computed tomography (PET/CT), and software fusion of PET and MR imaging data sets are increasingly used to facilitate diagnosis in clinical practice. Because MR imaging and PET often yield complementary information, PET/MR imaging holds promise to facilitate differentiation of tumor recurrence from radiation therapy–induced changes and complications. This review focuses on clinical applications of DW and PET/MR imaging in the irradiated neck and discusses the added value of multiparametric imaging to solve diagnostic dilemmas. Radiologists should understand key features of radiation therapy–induced tissue alterations and potential complications seen at DW and PET/MR imaging, including edema, fibrosis, scar tissue, soft-tissue necrosis, bone and cartilage necrosis, cranial nerve palsy, and radiation therapy–induced arteriosclerosis, brain necrosis, and thyroid disorders. DW and PET/MR imaging also play a complementary role in detection of residual and recurrent disease. Interpretation pitfalls due to technical, functional, and metabolic phenomena should be recognized and avoided. Familiarity with DW and PET/MR imaging features of expected findings, potential complications, and treatment failure after radiation therapy increases diagnostic confidence when interpreting images of the irradiated neck. *Online supplemental material is available for this article.*

SA-CME LEARNING OBJECTIVES

After completing this journal-based SA-CME activity, participants will be able to:

- Recognize key imaging features of radiation therapy–induced changes and complications in the head and neck.
- Describe diffusion-weighted and PET/MR imaging findings of residual and recurrent tumors in the head and neck.
- Discuss potential pitfalls of image interpretation and how to avoid them.

See www.rsna.org/education/search/RG.

Introduction

Over 95% of malignant head and neck tumors in adults are squamous cell carcinomas (SCCs), while the remaining 5% comprise various other histologic types, such as thyroid cancers, adenoid cystic carcinoma, melanoma, lymphoma, chondrosarcoma, and other rare tumors. This review excludes thyroid and skin cancers and focuses on head and neck SCCs arising in the upper aerodigestive tract. Treatment decisions for patients with head and neck SCC are made in the setting of multidisciplinary tumor boards and are influenced by clinical parameters, histologic findings, primary versus recurrent disease, submucosal tumor extent, and presence of nodal or distant metastases and second primary tumors (1,2). Treatment options include surgery, radiation therapy, chemotherapy, or a combination thereof (2).

TEACHING POINTS

- Typical imaging findings include thickening of subcutaneous fat, retropharyngeal fat, and platysma; characteristic reticulated soft-tissue enhancement; and major airway narrowing, especially in the supraglottic larynx. These findings are limited to the radiation therapy port and are well appreciated on contrast-enhanced fat-saturated T1-weighted MR images. On DW images, normal or increased diffusion due to edema is observed. On PET/MR images, FDG uptake can be variable.
- Because of their abundant collagen fibers and stromal fibrin, scars typically show low signal intensity on T1- and T2-weighted MR images, fairly regular thickness, elongated shape, and a flat edge with a retracted margin; there is often deformation of adjacent tissues and mucosal retraction due to the underlying desmoplastic reaction. Contrast enhancement can be strong in immature scars and faint or absent in long-standing mature scars. At DW imaging, scar tissue has low signal intensity on $b = 0$ sec/mm^2 and $b = 1000$ sec/mm^2 images and a low ADC.
- In early stages of soft-tissue necrosis, local mucosal destruction can be detected endoscopically. MR imaging findings are subtle, and the normally enhancing mucosal line appears discontinuous. In more advanced stages, soft-tissue ulcerations appear at CT and MR imaging as large, well-delineated, "punched-out" defects that lack the characteristic enhancing mucosal layer. Tiny air-filled pockets near the ulcerated area and fistula formation are common.
- The imaging characteristics of recurrent tumors at DW and PET/MR imaging are similar to those of primary tumors. Recurrent head and neck SCCs are seen as soft-tissue masses with high FDG uptake, moderately high T2 signal intensity, and moderate to high contrast enhancement. At DW imaging, they show restricted diffusion with low ADCs (most often $<1.3 \times 10^{-3}$ mm^2/sec), which allows differentiation from benign radiation therapy–induced changes (ADC $>1.6–1.8 \times 10^{-3}$ mm^2/sec).
- Inflammatory or infectious conditions can lead to false-positive PET findings in the irradiated neck, and correlation with DW imaging findings can help solve the diagnostic dilemma. In clinical practice, no PET/MR imaging examination should be performed without knowledge of clinical findings, especially if an infectious event is suspected.

Radiation therapy for head and neck tumors includes external beam radiation therapy and brachytherapy. While external beam radiation therapy delivers photons, electrons, or protons produced by external radiation sources, brachytherapy is performed with radiation sources implanted in the patient. Intensity-modulated radiation therapy (IMRT) is currently the preferred radiation therapy option for the head and neck. It uses computer-controlled linear accelerators that deliver high radiation doses (photon radiation therapy) to the tumor while minimizing the dose to surrounding normal tissues and critical organs such as the parotid glands, optic nerve, and spine (2–10). Local control is thereby improved, and related morbidity is reduced. Proton beam radiation therapy uses high-energy protons; it is used for certain rare tumors (chordoma and chondrosarcoma of the skull base) and selected sinonasal or nasopharyngeal carcinomas. Because the protons have a large mass, scatter remains limited and allows sparing of surrounding tissues while the radiation dose is delivered to the tumor.

At IMRT, radiation doses delivered to tumors and lymph nodes documented at imaging and to high-risk areas (eg, suspected microscopic disease, postoperative tumor bed with positive margins or extranodal spread) are typically 62–70 Gy (5–9). Subclinical disease sites with negative imaging findings and intermediate risk for microscopic involvement receive a radiation dose of 59–63 Gy, while areas with lower risk for microscopic involvement receive 50–58 Gy. Critical tissues such as the brainstem, spinal cord, and optic pathway typically receive doses below 45–50 Gy (5–10). Determination of clinical target volumes and differentiation of intermediate- from low-risk areas depends on the location of the primary tumor and possible microscopic extension, with use of surgical and pathologic data from the literature and internationally recognized guidelines (5–9). Full manual contouring of desired head and neck IMRT targets by the radiation oncologist is a laborious process that requires up to several hours per patient (10,11); therefore, atlas-based segmentation methods are increasingly used to plan head and neck IMRT (11). As shown by several investigators (4,12,13), tissues exposed to radiation therapy undergo structural, functional, and metabolic changes. These changes can hamper early detection of recurrent disease.

Indications for imaging after radiation therapy include clinically suspected tumor recurrence and regular follow-up of high-risk patients (4,13–15). Interpreting imaging studies of the irradiated neck constitutes a diagnostic challenge because of radiation therapy–induced tissue alterations and complications, the variable appearances of recurrent tumors, and functional and metabolic phenomena that mimic disease. Therefore, contrast-enhanced computed tomography (CECT), morphologic magnetic resonance (MR) imaging, diffusion-weighted (DW) imaging, combined positron emission tomography and computed tomography (PET/CT), and software fusion of PET and MR imaging data are used in routine clinical practice. Because MR imaging and PET often yield complementary information (16), recently introduced hybrid PET/MR imaging systems (17–21) hold promise to facilitate differentiation of tumor recurrence from posttreatment complications.

This article reviews clinical applications of DW and PET/MR imaging in the irradiated neck and discusses the complementary role of these modalities in solving diagnostic dilemmas. We provide

Table 1: Reported ADCs of Primary and Recurrent Head and Neck SCCs

Study	Year	No. of Tumors	Mean ADC ± SD (× 10^{-3} mm^2/sec)	Minimum ADC ± SD (× 10^{-3} mm^2/sec)
Primary SCC				
Choi et al (28)	2011	47	1.22 ± 0.28	ND
Fruehwald-Pallamar et al (29)	2011	31	1.05 ± 0.21	ND
Nakajo et al (30)	2012	26	0.92 ± 0.19	ND
King et al (24)	2013	37	1.22 ± 0.21	ND
Varoquaux et al (26)	2013	24	1.02 ± 0.30	0.61 ± 0.29
Recurrent SCC				
Vandecaveye et al (15)	2007	15	1.11 ± 0.29	ND
Abdel Razek et al (31)	2007	30	1.17 ± 0.33	ND
Varoquaux et al (26)	2013	10	1.13 ± 0.41	0.73 ± 0.29
Tshering Vogel et al (32)	2013	46	1.2 ± 0.46	ND

Note.—All indicated values correspond to monoexponentially fitted total ADC values. ND = no data, SD = standard deviation.

a comprehensive approach to understanding key imaging features of radiation therapy–induced changes and complications seen at DW and PET/MR imaging, review the added value of DW and PET/MR imaging for detection of recurrent disease, and discuss interpretation pitfalls and how to avoid them.

DW and PET/MR Imaging

DW imaging is a functional MR imaging technique that enables depiction and quantification of the Brownian motion of water molecules in vivo (21–23). Because macromolecules, membranes, cell organelles, and fibers hinder free displacement (diffusion) of water molecules in biologic tissues, DW imaging enables detection of early pathologic changes. Restricted diffusion is a consequence of cytotoxic edema or increased cellularity. It is seen in a variety of pathologic conditions, including stroke, malignant hypercellular tumors, some benign tumors (Wharthin tumors), thrombi, inflammation, infection, and abscesses (14–16,21–27). In addition, normal lymphatic structures (Waldeyer ring and normal lymph nodes) also display restricted diffusion due to their inherently high cellularity. Increased diffusion of water molecules occurs in tissues with decreased cellularity, such as necrotic tissues and necrotic tumors, and in vasogenic edema (14,22,24–27).

The apparent diffusion coefficient (ADC) is a metric used for quantification at DW imaging. In clinical practice, ADCs (expressed in square millimeters per second) are calculated with use of software programs and are displayed as a parametric map. Most often, a monoexponential fitting (two *b* values) is used. The monoexponential fitting represents a rough approximation of true diffusion. Multiexponential models with several *b* values are more suitable for quantification; however, acquisition of DW images with multiple *b* values increases scan duration. In most head and neck imaging protocols, the higher *b* values used at DW imaging are 800–1000 sec/mm^2. Although calculation of ADCs depends on a variety of factors (eg, MR imaging equipment; magnetic field heterogeneity; air, bone, and soft-tissue interfaces; and section thickness), ADC measurements have been shown to be reproducible, with excellent intra- and interobserver reproducibility (26). ADCs in tumors depend on histologic characteristics. ADCs in thyroid cancer are 1.3–3 × 10^{-3} mm^2/sec; in head and neck SCC, they are 0.6–1.5 × 10^{-3} mm^2/sec, with a mean of 0.9–1.2 × 10^{-3} mm^2/sec (Table 1). ADCs are even lower in head and neck lymphoma, with reported values of 0.5–0.9 × 10^{-3} mm^2/sec (14–16,18,22,27).

Furthermore, as recently reported, ADCs in head and neck SCC also depend on the degree of tumor differentiation. Poorly differentiated head and neck SCCs tend to have lower ADCs than do well-differentiated tumors (26,27). This finding has been attributed to the higher nuclear-cytoplasmic ratio seen in poorly differentiated lesions compared to the small foci of liquefactive necrosis typically seen in well-differentiated tumors (14,16,18,22,26,27). Therefore, evaluation of patients who have undergone radiation therapy for malignant head and neck tumors should take the histologic characteristics of treated tumors into consideration. Although there is no generally applicable ADC threshold for detection of

tumor recurrence, a mean ADC of less than 1.3×10^{-3} mm²/sec is generally acknowledged to indicate restriction, and in the irradiated neck, such low ADCs indicate recurrent disease (14,16,22,24,26,27). Nevertheless, as some overlap in ADC values may exist between benign and malignant conditions, interpretation of ADCs should be done carefully and in conjunction with morphologic findings.

Fluorine 18 fluorodeoxyglucose (FDG) is a glucose analog taken up by metabolically active tumor cells, and uptake is mainly related to the proliferation rate and viability of neoplastic cells. As the radiotracer becomes entrapped in cells after phosphorylation, FDG PET allows quantification of glucose metabolism. FDG PET/CT has been shown to have a high sensitivity and high negative predictive value for detection of head and neck SCC (16,33,34). Although FDG PET/CT rarely adds additional information to MR imaging and CECT regarding the tumor stage in primary head and neck SCC, it is of undisputed value for assessment of lymph node metastases, distant metastases, and synchronous primary tumors; identification of unknown primary tumors; posttreatment surveillance; and detection of recurrent disease (21,35). Nevertheless, increased FDG uptake can also be seen in a variety of benign conditions with high glucose metabolism (eg, inflammatory nodes, granulation and scar tissue, and Warthin tumors); this increased FDG uptake may lead to false-positive imaging findings (34,36).

Quantification of tracer uptake at PET is commonly performed by using the standardized uptake value (SUV). The SUV is a semiquantitative metric calculated by dividing the tissue radioactivity concentration at a certain time by the injected radioactivity extrapolated to the same time and the body weight. The SUV can be calculated pixel-by-pixel, yielding a parametric image, or it can be calculated over a region of interest. Although SUV measurements depend on multiple factors (ie, patient status, scanner calibration, data acquisition, reconstruction parameters, and choice of regions of interest), quantification according to mean and maximum SUVs is widely used in clinical practice because SUV measurements are easily obtained on the computer screen during image interpretation and there is excellent intra- and interobserver reproducibility (26). Most head and neck SCCs have high mean and maximum SUVs (>3; typically 5–9 for mean SUV and 6–16 for maximum SUV) (18,26, 28–30,33–35,37–41) (Table 2). However, small metastatic lymph nodes, necrotic tumors, and tumors with an inherently low proliferation rate may not be FDG avid and thus may have low SUVs, whereas inflammatory processes may show high FDG uptake and high SUVs (see the section on "Pitfalls") (24,34,36,42–45). Therefore, it is generally accepted that characterization of a lesion using an SUV threshold alone is not adequate, particularly in the irradiated neck, and correlation with CECT, MR imaging, or DW imaging findings is essential.

Because of high lesion-to-background contrast, images obtained by applying gray-scale inversion to DW imaging datasets acquired with *b* of 1000 sec/mm² visually resemble FDG PET images (16,26). However, because DW imaging and PET have completely different biophysical and biochemical foundations and ADCs and SUVs are independent biomarkers (16,26), the information provided by the two techniques is complementary. This complementarity has led to increasing use of multimodality image fusion and development of hybrid PET/MR imaging systems.

Hybrid PET/MR Imaging and Multimodality Image Fusion

Recently introduced hybrid PET/MR imaging systems enable acquisition of anatomic, functional, and metabolic information during the same session (17–21). Currently, three types of hybrid systems exist: simultaneous PET/MR imaging (PET and MR imaging subsystems integrated in the same gantry), sequential PET/MR imaging (two separate imaging units in the same room that use a common rotating table), and sequential PET/CT and MR imaging (separate PET/CT and MR imaging units in two adjacent examination rooms, with a mobile patient table that can be docked to either of the two imaging units). Attenuation correction for PET data used to calculate SUVs is done using MR imaging–based attenuation correction maps in the first two systems, whereas trimodality PET/CT and MR imaging uses classic CT-based attenuation correction methods.

Calculating SUVs from MR imaging datasets constitutes a challenge because signal intensity on MR images is not directly associated with attenuation values of biologic tissues. Transformation of MR imaging datasets into attenuation maps for PET is currently a field of intense research. Although several groups have shown a strong correlation between SUVs at PET/MR imaging and PET/CT (18,21,46,47), it has been suggested that SUVs of focal lesions and organs are underestimated at PET/MR imaging compared with at PET/CT (18,21,46,47). Although quantification in PET/MR imaging systems has implications for everyday clinical work, discussion of quantification issues related to MR imaging–based attenua-

Table 2: Reported Mean and Maximum SUVs of Primary and Recurrent Head and Neck SCCs at PET/CT

Study	Year	No. of Tumors	Mean SUV ± SD	Maximum SUV ± SD
Primary SCC				
Machtay et al (37)	2009	60	8.5	ND
Haerle et al (38)	2010	294	ND	10.7 ± 4.6
Imsande et al (39)	2011	18	ND	12.5 ± 8.7
Choi et al (28)	2011	47	5.2 ± 2.0	12.0 ± 5.5
Fruehwald-Pallamar et al (29)	2011	31	ND	16.5 ± 12.1
Nakajo et al (30)	2012	26	ND	15.5 ± 6.7
Higgins et al (40)	2012	88	7.0	15.4
Varoquaux et al (26)	2013	24	10.7 ± 3.7	14.1 ± 4.9
Varoquaux et al (18)*	2014	32	5.5 (4.2, 8.7),† 7.7 (5.4, 11.5)	6.6 (5.5, 10.9),† 8.7 (7.3. 15.1)
Recurrent SCC				
Wong et al (41)	2002	69	5.8 ± 3.7‡	ND
Varoquaux et al (26)	2013	10	7.9 ± 3.5	9.9 ± 4.3
Varoquaux et al (18)*	2014	32	5.5 (4.2, 8.7),† 7.7 (5.4, 11.5)	6.6 (5.5, 10.9),† 8.7 (7.3, 5.1)

Note.—Numbers in parentheses represent data obtained at interquartile intervals.
ND = no data, SD = standard deviation.
*Data include primary and recurrent tumors; SDs not provided.
†Measured at PET/MR imaging.
‡Measured at PET.

tion correction versus CT-based attenuation correction and factors influencing SUVs is beyond the scope of this article (18,21,46–48).

In multimodality image fusion, a color or gray-scale functional image (eg, PET or DW) is superimposed on a corresponding anatomic MR image. DW data obtained with *b* of 1000 sec/mm^2 or PET data acquired independently of MR imaging data can be fused with it by using commercially available software algorithms, whereas in hybrid PET/MR imaging systems, image fusion is achieved by use of hardware fusion.

Key Findings at MR, DW, and PET/MR Imaging

The radiologist performing imaging of the head and neck in patients who have undergone radiation therapy must differentiate between expected changes after radiation therapy, potential complications of radiation therapy, and residual or recurrent tumor (4,13,15,49). High-dose radiation therapy required for treatment of malignant head and neck tumors affects normal tissues included in the radiation therapy portal (12). Early effects typically occur after the first 1–2 weeks after the start of radiation therapy (49). They are seen in tissues with rapid cell renewal (epithelial and hematopoietic stem cells), where frequent mitosis is required to maintain organ function (12). Most acute effects (mucositis and erythema) are self-limiting and reversible.

Late effects tend to occur months or years after completion of radiation therapy and affect tissues with low mitotic activity, such as neural, fatty, and vascular tissue; bone; and cartilage. Late effects are caused by damage to connective tissue cells and the endothelial lining of small blood vessels (12). Damage to microvasculature leads to secondary cell death due to nutrient deprivation. Late effects of radiation therapy include edema, nonreversible fibrosis, progressive parenchymal destruction, and subsequent organ atrophy. Radiation therapy–induced fibrosis is associated with expression of inflammatory cytokines (transforming growth factor [TGF]–β), which stimulate fibroblast proliferation, differentiation into fibrocytes, and collagen production. Fibrosis due to radiation therapy is a dynamic process with an apparently uncontrolled remodeling phase and increased severity over time (49,50). The extent of radiation therapy–induced fibrosis and organ atrophy may differ from one patient to another, even if identical radiation therapy treatments are used (50), and it has been suggested that genetic factors, additional chemotherapy, corticosteroid administration, and fractionation schedule may contribute to variability in individual radiosensitivity (51).

Combined treatment modalities (ie, radiation therapy with surgery or chemotherapy) can further lead to increased severity of fibrosis (51,52). All of these factors may explain why radiation therapy–induced tissue damage depicted at cross-sectional imaging can differ in severity among patients.

Expected Changes after Radiation Therapy

Mucositis, Dermatitis, Soft-Tissue Edema, and Fibrosis.—Edema is a common finding in the irradiated neck, with a reported prevalence of 75%–90% at 3 months after radiation therapy (53). Edema is mainly caused by impaired lymphatic flow (secondary lymphedema) due to neck fibrosis and formation of scar tissue. Radiation therapy–induced superficial lymphedema affects the anterior neck and submental, facial, and, less often, intraoral areas. Deep-space lymphedema typically affects the visceral, retropharyngeal, and carotid spaces (54). Both types of lymphedema most often coexist. Contrast-enhanced MR images obtained during the first 9 months after radiation therapy frequently show skin thickening and enhancement (dermatitis) and intense mucosal enhancement corresponding to mucositis (4,13). Typical imaging findings include thickening of subcutaneous fat, retropharyngeal fat, and platysma; characteristic reticulated soft-tissue enhancement; and major airway narrowing, especially in the supraglottic larynx (13,23,54). These findings are limited to the radiation therapy port and are particularly well appreciated on contrast-enhanced fat-saturated T1-weighted MR images (Fig 1). At DW imaging, normal or increased diffusion due to edema is observed. At PET/MR imaging, FDG uptake can be variable (23,31). In patients with severe mucositis, intense FDG uptake can render differentiation from residual tumor difficult (55). A nasogastric tube or tracheostomy cannula can also lead to increased FDG uptake due to local irritation of the pharyngeal, esophageal, and tracheal mucosa. However, absence of an obvious mass at morphologic MR imaging and normal or increased diffusion at DW imaging facilitates diagnosis of benign inflammatory FDG uptake.

Scar Tissue.—Six weeks to 1 year after radiation therapy, some patients develop extensive fibrosis, with a hypertrophic scar formed beneath the mucosa that was initially involved by tumor. This hypertrophic scar can be detected at MR and PET/MR imaging and typically is located in the muscular structures of the floor of the mouth, pharynx, larynx, neck, or masticator space. It is seen whenever the tumor showed deep invasion at pretreatment MR imaging (56). Hypertrophic scar tissue is the result of abnormal wound healing, with loss of the control mechanisms that regulate tissue repair and regeneration. Histologically, scar tissue can be subdivided into mature and immature scars. Immature scars caused by radiation therapy are characterized by variable amounts of fibroblasts, fibrocytes, fibrin, and collagen, whereas mature scars are mainly composed of stromal fibrin and collagen bundles. Scars induced by radiation therapy contain atypical fibroblasts (so-called radiation fibroblasts) with triangular or bizarre shapes and "smudged" hyperchromatic nuclei, but these features do not imply biologic aggressivity (57).

The reported MR imaging appearances of scars due to radiation therapy, surgery, laser resection, or a combination of these techniques are similar (54,56,58–62). Because of their abundant collagen fibers and stromal fibrin, scars typically show low signal intensity on T1- and T2-weighted MR images, fairly regular thickness, elongated shape, and a flat edge with a retracted margin (54,56,58–62); there often is deformation of adjacent tissues and mucosal retraction due to the underlying desmoplastic reaction (Fig 2). Contrast enhancement can be strong in immature scars and faint or absent in long-standing mature scars. At DW imaging, scar tissue has low signal intensity on images obtained with b of 0 sec/mm^2 and b of 1000 sec/mm^2 images and low ADCs (Fig 2) (58,60). Over time, the signal intensity of the scar further decreases and becomes even lower with all sequences, especially T2-weighted MR imaging sequences. This low T2 signal intensity is characteristic of benign scar tissue and should be differentiated from intermediate T2 signal intensity ("evil gray") encountered in head and neck SCC (31,52–64). As opposed to benign scar tissue, residual or recurrent head and neck SCC lesions manifest as expansive, poorly delineated, infiltrative areas with T2 signal intensity similar to that of untreated tumor and show moderate to strong enhancement after intravenous administration of gadolinium chelate contrast agent (58–62). Recently, it has been suggested that residual masses composed entirely of scar tissue are associated with low likelihood of tumor recurrence, independent of scar size (56). FDG uptake in radiation therapy–induced scars is variable. Although FDG uptake in early immature scars can be prominent because of increased glucose metabolism (Fig 3), once the scar is mature, no significant FDG uptake is observed (Fig 2).

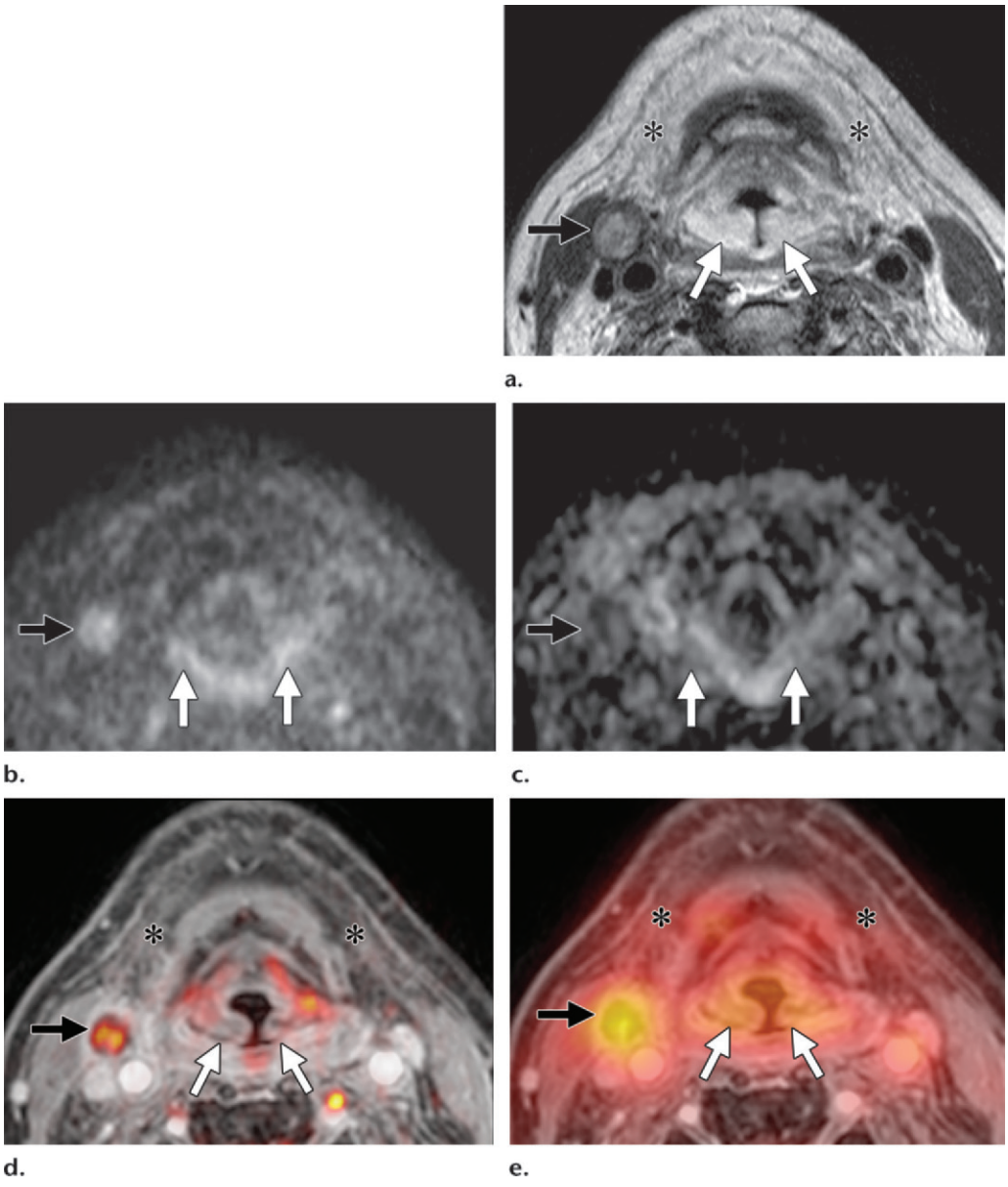

Figure 1. Radiation therapy–induced fibrosis and edema 4 months after radiation therapy for supraglottic SCC. Axial T2-weighted MR image **(a)**, DW image (b = 1000 sec/mm^2) **(b)**, ADC map **(c)**, fused DW (b = 1000 sec/mm^2)–gadolinium-enhanced fat-saturated T1-weighted MR image **(d)**, and fused PET–gadolinium-enhanced fat-saturated T1-weighted MR image **(e)** show edema and fibrosis in the anterior neck (* in **a, d,** and **e**) and aryepiglottic folds (white arrows), with airway narrowing. No restricted diffusion is seen in the larynx in **b** and **c**, and there is minor FDG uptake in the larynx in **e**. Restricted diffusion and high focal FDG uptake are seen in a histologically proven residual level II–III lymph node metastasis (black arrow).

Sialadenitis and Xerostomia.—Radiation therapy–induced sialadenitis is a major cause of morbidity after radiation therapy (12,65). Sialadenitis leads to xerostomia, which predisposes to fulminant caries and delayed osteoradionecrosis. Although the exact mechanism of radiation therapy–induced sialadenitis is not completely understood, cell-mediated immune mechanisms are thought to play a main role in pathogenesis (65). In early-stage disease, MR imaging reveals major gland edema (particularly well depicted on fat-saturated T2-weighted and short inversion time inversion-recovery [STIR] MR images) and increased vascularization (best seen on contrast-enhanced fat-saturated T1-weighted MR images) (54). Diffusion is slightly restricted (decreased ADCs) throughout the gland, and FDG uptake is increased (moderately high–high SUVs). Diffuse FDG uptake in the salivary glands is nonspecific and can also occur in patients who have not undergone radiation therapy and those without salivary gland disease (36,44,66). In fact, it is seen in many patients undergoing pretreatment FDG PET/CT of the head and neck. Unilateral

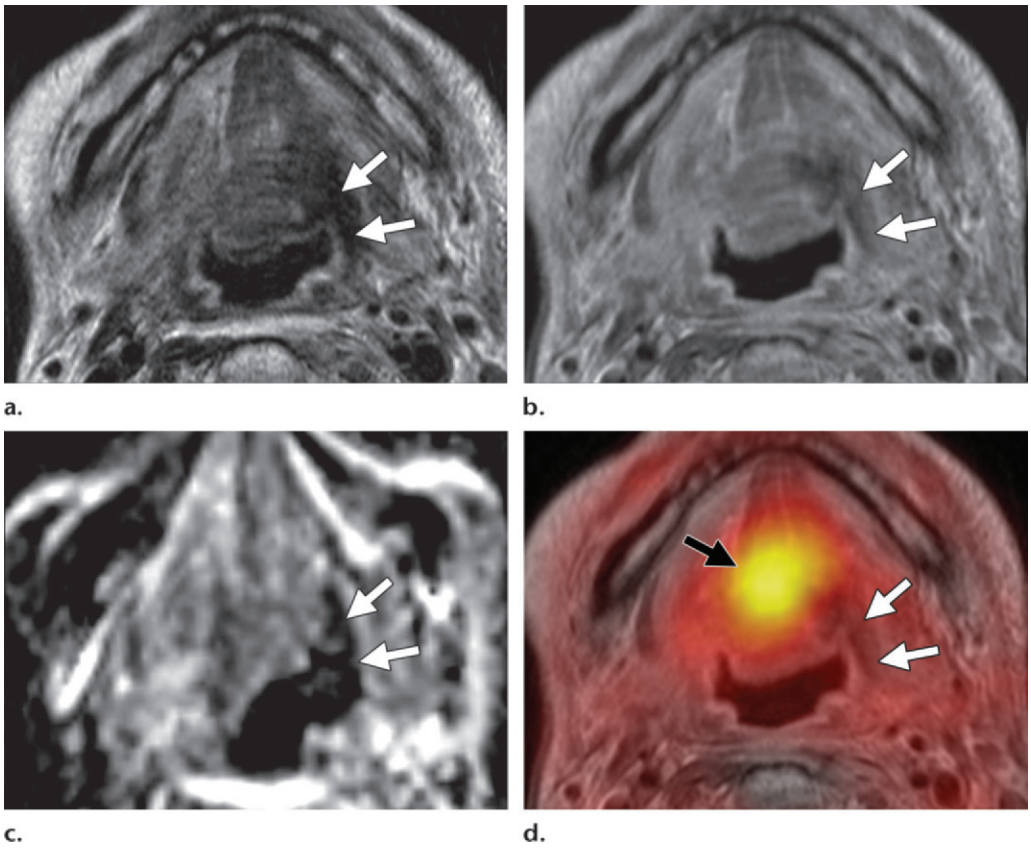

Figure 2. Mature scar tissue 10 months after radiation therapy and chemotherapy for an SCC in the left base of the tongue. Axial T2-weighted MR image **(a)**, gadolinium-enhanced T1-weighted MR image **(b)**, ADC map **(c)**, and fused FDG PET–gadolinium-enhanced T1-weighted MR image **(d)** show asymmetry of the base of the tongue, with soft-tissue and mucosal retraction due to desmoplastic reaction on the left side and low-signal-intensity mature scar tissue (white arrows). Focal midline FDG uptake seen in **d** (black arrow) is due to muscle activity. The geniohyoid muscles are normal. Follow-up images obtained 18 months later confirmed no recurrence of SCC.

inclusion of major salivary glands in the radiation therapy port may lead to asymmetric FDG uptake and unilateral restricted diffusion. Correlation with morphologic MR images, PET/MR image fusion, and knowledge of the radiation therapy port helps avoid misdiagnosis. After 9–12 months, progressive gland atrophy leads to fatty replacement and decreasing FDG metabolism with progressively decreasing SUVs. IMRT and dose painting can be used to spare parotid and submandibular gland function without compromising treatment efficacy.

Replacement of Hematopoietic Marrow by Fatty Marrow and Activation after Chemotherapy.—Damage to bone marrow cells after radiation therapy results in acute edema followed by fatty replacement and endosteal fibrosis (12,13). At radiation doses higher than 10 Gy (67), all irradiated marrow spaces (ie, cervical spine, mandible, bony skull base, ossified laryngeal cartilages) show persistent signs of injury from radiation therapy at PET/MR imaging. MR imaging demonstrates inflammatory changes (increased signal intensity on STIR images and increased enhancement on gadolinium-enhanced images) as early as 7 days after radiation therapy (68). At 4 weeks after radiation therapy, fatty replacement and early fibrosis are common (high signal intensity on T1-weighted MR images and persistent enhancement) (68). However, enhancement of fatty marrow decreases over time.

FDG uptake in irradiated marrow is usually lower than in the liver. However, recovering bone marrow activity after chemotherapy and treatment with certain agents (eg, granulocyte colony-stimulating factor [GCSF]) can lead to extensive, diffuse, homogeneous FDG uptake (Fig 4) (69). Its characteristic appearance and rapid decrease within 1 month after treatment allow differentiation from metastatic disease.

Physiologic Functional and Metabolic Findings.—High physiologic FDG uptake and restricted diffusion typically occur in normal lymphoid tissue within the Waldeyer ring in patients with or without a history of radiation therapy (16,27). Because high FDG uptake and restricted diffusion at PET/

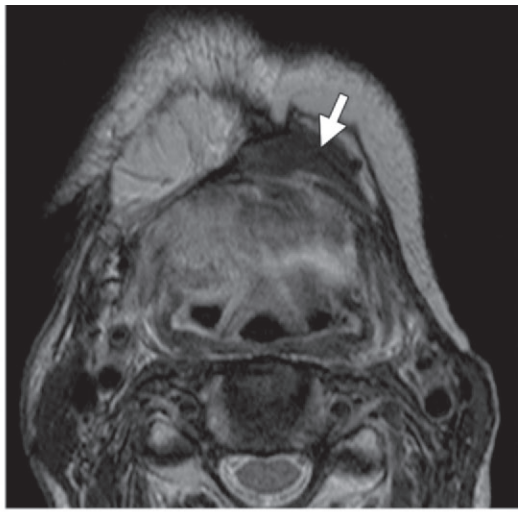

a.

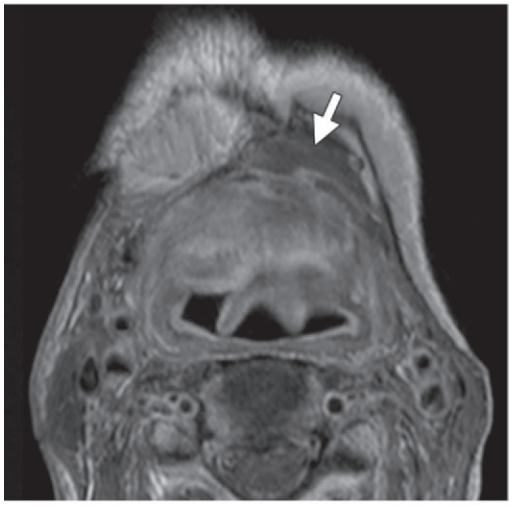

b.

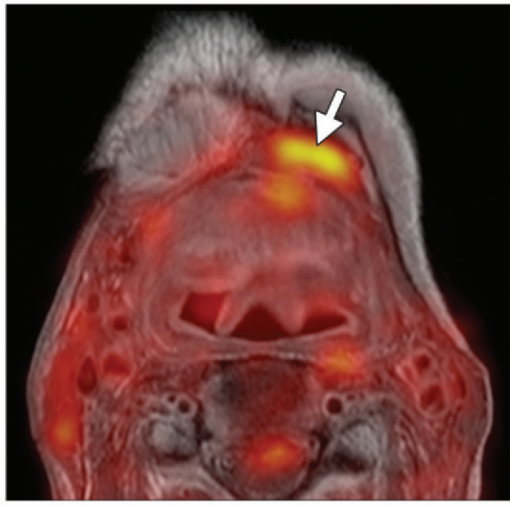

c.

Figure 3. PET/MR imaging appearance of immature scar tissue 4 months after radiation therapy and surgery for an SCC in the floor of the mouth. Axial T2-weighted **(a)**, gadolinium-enhanced T1-weighted **(b)**, and fused FDG PET–gadolinium-enhanced T1-weighted **(c)** MR images show an area of scar tissue (arrow) with low signal intensity in **a**, enhancement in **b**, and focal FDG uptake in **c**. DW images (not shown) demonstrated no restricted diffusion. Follow-up MR images showed no change in scar tissue appearance, whereas FDG uptake disappeared at follow-up imaging.

Figure 4. Bone marrow activation 2 months after radiation therapy and chemotherapy for a lymphoma at the base of the tongue. Sagittal FDG PET image from PET/MR imaging shows increased FDG uptake in the dorsolumbar spine and sternum due to bone marrow activation (arrows indicate radiation port). No FDG uptake is seen in the cervical spine. Follow-up images obtained 1 month later showed decreasing FDG uptake, and PET/CT images obtained 18 months after the image shown demonstrated no findings of recurrent disease.

MR imaging can be mistaken for recurrent tumor in the nasopharynx and oropharynx, detailed evaluation with use of morphologic MR imaging sequences and, in cases of asymmetric uptake, endoscopy is mandatory for correct diagnosis (Fig 5).

High physiologic nonspecific FDG uptake can also be seen in the tongue, laryngeal muscles, and cervical muscles in both the irradiated and nonirradiated neck (44). Muscle uptake of FDG is generally linear and can be traced from the origin of the muscle to its insertion. Nevertheless, focal FDG uptake by muscle can constitute a pitfall on

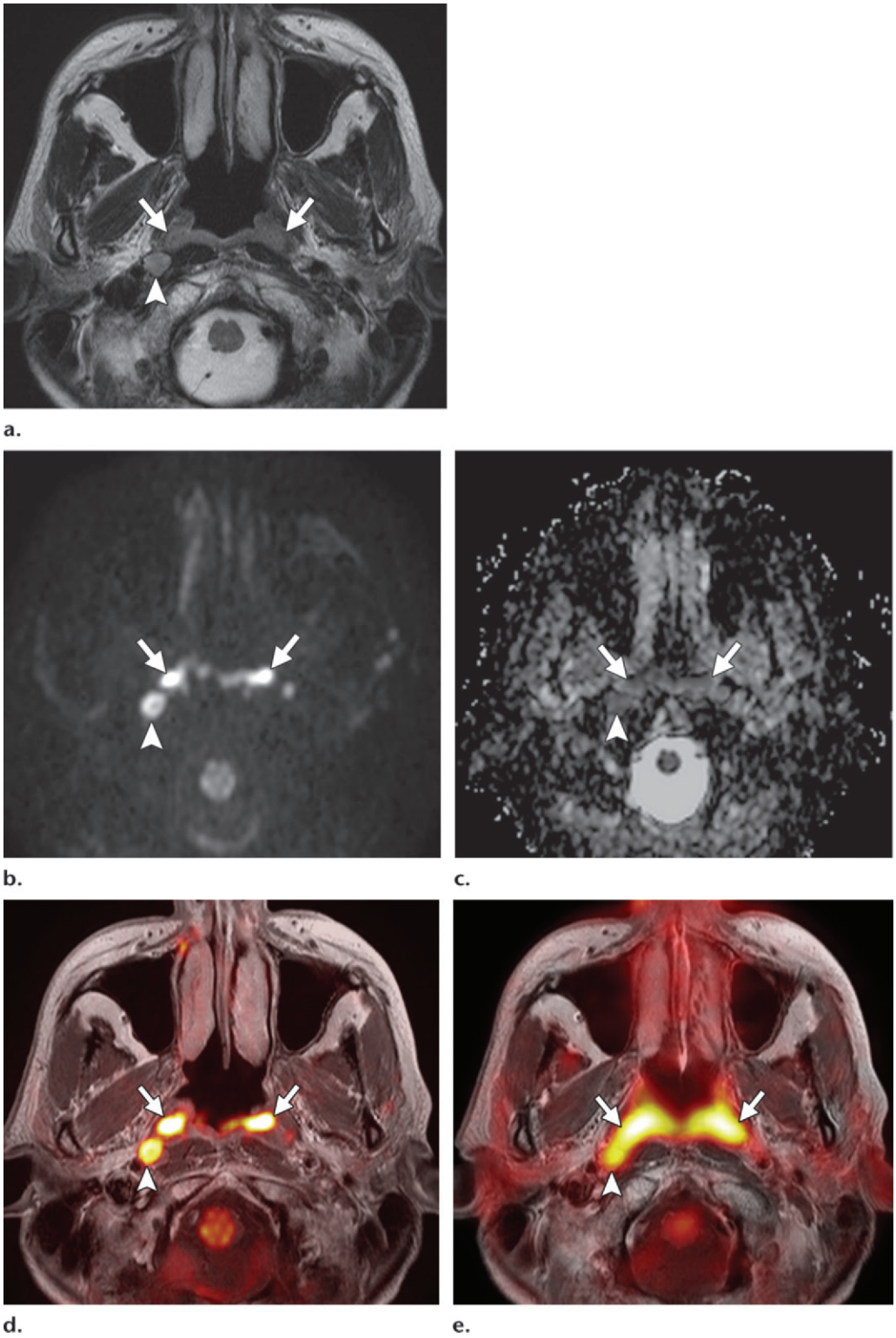

Figure 5. High FDG uptake and restricted diffusion in lymphatic tissue and an enlarged retropharyngeal lymph node mimicking recurrent disease 3 years after radiation therapy and chemotherapy for a right-sided oropharyngeal SCC. **(a)** Axial T2-weighted MR image shows slightly hypertrophic but otherwise normal lymphatic tissue in the nasopharynx (arrows) and an 8-mm retropharyngeal node (arrowhead). **(b–d)** Axial DW image (b = 1000 sec/mm^2) **(b)**, ADC map **(c)**, and fused DW (b = 1000 sec/mm^2)–gadolinium-enhanced T1-weighted MR image **(d)** show restricted diffusion in the nasopharynx (arrows) and retropharyngeal node (arrowhead). Recurrent disease cannot be ruled out, especially because of the retropharyngeal node enlargement. **(e)** Axial fused PET–gadolinium-enhanced T1-weighted MR image shows increased FDG uptake in the nasopharynx (arrows) with apparent retropharyngeal extension (arrowhead). The apparent extension is caused by lower resolution at PET compared with at MR imaging. The DW and PET/MR imaging findings were considered suspicious for recurrent disease, and biopsies of adenoid tissue and the retropharyngeal node were performed. Biopsy results and follow-up images obtained 20 months later were negative for recurrence.

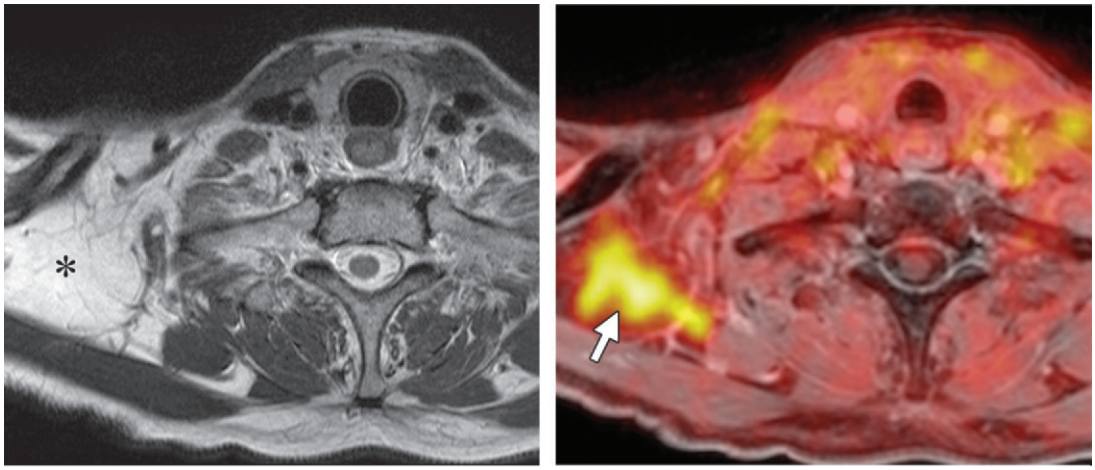

Figure 6. High physiologic brown fat metabolism with characteristic FDG uptake 9 months after radiation therapy and chemotherapy for an SCC at the base of the tongue. Axial T2-weighted MR image **(a)** and fused PET–gadolinium-enhanced fat-saturated T1-weighted MR image **(b)** show supraclavicular fatty tissue (∗ in **a**) with high FDG uptake (arrow in **b**). DW imaging findings (not shown) were normal.

axial images. Therefore, coronal and/or sagittal imaging planes and good fusion of PET and MR images are essential for correct diagnosis. DW images typically show no restricted diffusion.

Prominent physiologic FDG uptake in brown fat is a characteristic finding in the lower neck and supraclavicular and paraspinal regions, especially in children and younger patients (36,66,69). Brown fat is also seen more often in women than in men. Because brown fat is innervated by the sympathetic nervous system, administering oral propranolol or maintaining a warm ambient temperature during the uptake phase can reduce brown fat uptake of FDG. High FDG uptake due to increased brown fat metabolism can be seen before and after radiation therapy; it is not a consequence of radiation therapy. It can be confused with metastatic lymph nodes, and precise image fusion and correlation with morphologic MR images are mandatory for correct diagnosis (Fig 6). Poor image fusion caused by patient motion between PET and morphologic MR imaging (see the section on "Miscoregistration Artifacts") may occasionally render interpretation of findings more difficult, particularly in patients with brown fat in atypical locations such as the mediastinum.

Complications after Radiation Therapy

Soft-Tissue Necrosis and Granulation Tissue.— Delayed radiation therapy–induced soft-tissue necrosis most often occurs within 2 years after radiation therapy (70) and can be seen secondary to any form of radiation therapy. Although radiation therapy–induced soft-tissue necrosis tends to heal spontaneously, extensive necrosis may occasionally require surgical treatment (13). Radiation therapy–induced soft-tissue necrosis is typically seen at the initial tumor site. It is caused by vascular and lymphatic vessel damage that leads to formation of hypoxic hypovascular tissue, and this "fragile" tissue is prone to necrosis and subsequent infection (71–73). Soft-tissue necrosis in the head and neck is typically associated with laryngeal or pharyngeal ulcer and occasionally with fistula formation (13,71) (Fig 7). At histologic analysis, the beds of radiation therapy–induced ulcers are surrounded by necrotic debris, granulation tissue, fibrosis, and fibrinoid necrosis of small arteries (55).

In early stages, local mucosal destruction can be detected endoscopically. MR imaging findings are subtle, and the normally enhancing mucosal line appears discontinuous (72). In more advanced stages, soft-tissue ulcerations are seen at CT and MR imaging as large, well-delineated, "punched-out" defects (Fig 7, Fig E1 [online]) and may lack the characteristic enhancing mucosal layer (32, 71–73). Tiny air-filled pockets near the ulcerated area and fistula formation are common (13,71,72). Extensive soft-tissue necrosis can extend into the skull base, parapharyngeal space, and carotid space and may lead to life-threatening carotid rupture (73). Similar to the imaging appearances of most radiation therapy–induced tissue alterations, MR imaging features of soft-tissue necrosis include higher T2 signal intensity and higher ADC values than those of recurrent head and neck SCC (15,31,32,60). After administration of gadolinium contrast agent, necrotic areas show no enhancement (72). Focal FDG uptake around the necrotic area is common because of coexisting inflammation with granulation tissue, and measured SUVs can be high. Therefore, high focal FDG uptake due to granulation

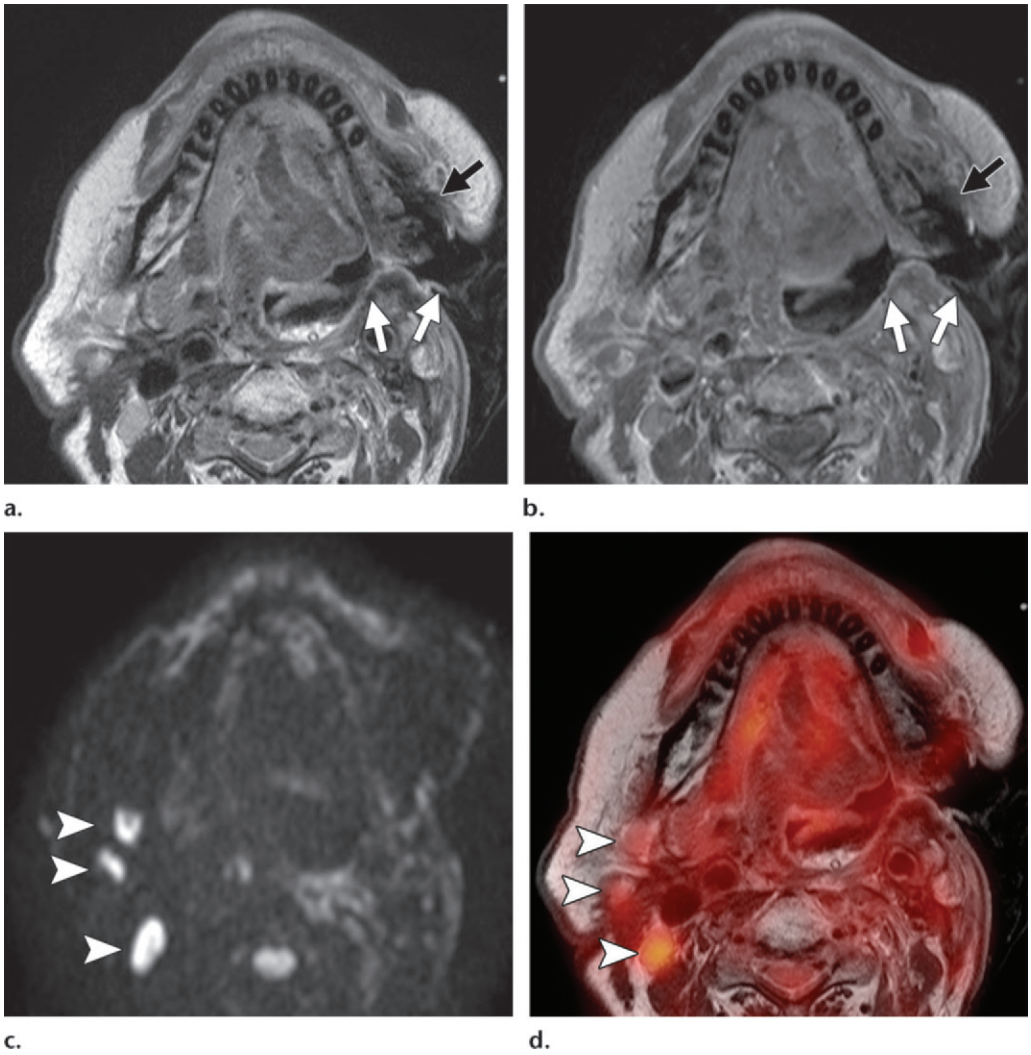

Figure 7. Soft-tissue necrosis with a pharyngocutaneous fistula in a woman who underwent radiation therapy and chemotherapy 5 years previously for an SCC in the left tonsil. Axial T2-weighted MR image **(a)**, gadolinium-enhanced T1-weighted MR image **(b)**, DW image (b = 1000 sec/mm^2) **(c)**, and fused PET–T2-weighted MR image **(d)** show ulceration of the left tonsillar fossa, with a pharyngocutaneous fistula (white arrows in **a** and **b**) due to extensive soft-tissue necrosis. Note the extension of soft-tissue necrosis around the denuded necrotic mandible on the left side (black arrow in **a** and **b**). No restricted diffusion or abnormal FDG uptake surrounds the area of soft-tissue necrosis. The level II lymph nodes seen on the right side (arrowheads in **c** and **d**) show restricted diffusion and variable FDG uptake. Mucous secretions with air-fluid level are seen in the oropharynx. Ultrasonographic (US) images of the neck (not shown) showed inflammatory lymph nodes. The patient was treated conservatively, and follow-up images obtained 12 months later confirmed benign soft-tissue necrosis and benign lymph nodes.

tissue is nonspecific and can lead to false-positive PET findings (55) (Fig E1 [online]).

In the presence of widespread granulation tissue, diffuse enhancement surrounding the necrotic area can be seen on T1-weighted MR images (Fig 7). Because tumor recurrence, particularly necrotic tumors, could be confused with benign soft-tissue necrosis, careful analysis of DW and PET/MR images is mandatory, and recurrent disease should be suspected whenever a nodular enhancing mass with restricted diffusion is seen in the periphery of a necrotic lesion. Because FDG uptake can be normal in necrotic tumors (see the section on "Pitfalls"), absent uptake does not exclude recurrent disease. Therefore, correlation with clinical findings, short-term follow-up examinations, and biopsy (when necessary) can help solve these diagnostic dilemmas. Nevertheless, it has been suggested that in patients with radiation therapy–induced soft-tissue necrosis with mucosal ulceration, if no contrast enhancement is seen at imaging and there is no clinical evidence of recurrence, soft-tissue necrosis is most likely benign (71) (Fig 7).

Osteoradionecrosis and Chondroradionecrosis.—Bone and cartilage necrosis most often affects the laryngeal cartilages, hyoid bone, mandible, and cervical spine (74–82). Osteoradionecrosis and chondroradionecrosis are associated

with intense FDG uptake (33,55), which makes differentiation from recurrent tumor difficult unless high-resolution morphologic MR and DW images are carefully analyzed.

Although osteoradionecrosis usually occurs 5–15 years after radiation therapy, some authors have found that time to diagnosis after completion of radiation therapy can range from 4 to 228 months and averages 18 months (74). Standard fractionation and radiation therapy doses of 62–70 Gy (12,75) are associated with increased risk for developing osteoradionecrosis (5%–15%). Patients who undergo IMRT tend to develop less severe osteoradionecrosis compared with patients treated with conventional radiation therapy (76). Osteoradionecrosis is a consequence of chronic tissue hypoxia combined with infectious or inflammatory events (eg, dental extraction, periodontal disease, or alveolitis) (75,77). Depending on the location of the radiation therapy port, osteoradionecrosis may affect the mandible, maxilla, skull base, or cervical spine. In the mandible, the molar and retromolar areas are preferentially affected. Osteoradionecrosis may occur in isolation or in association with recurrent disease.

Osteoradionecrosis is a predisposing factor for infection (13,78–81). Most cases of osteoradionecrosis are not detected clinically before complications such as marked trismus, infection, instability, or pathologic fractures occur (13,78–81). Osteoradionecrosis has a variable appearance at MR imaging, including bone marrow abnormalities (ie, edema with low signal intensity on T1-weighted images and high signal intensity on T2-weighted and STIR MR images or an intraosseous abscess with intense rim enhancement and gas-filled sequestra), cortical bone abnormalities (ie, erosion, disruption, fragmentation), pathologic fractures, and soft-tissue changes (ie, gingival ulcerations, deep-space edema, and myositis) (13,78–81). Diagnosis of osteoradionecrosis can be challenging at MR imaging in the absence of a straightforward abscess or mucosal ulcerations, as the conspicuity of air inclusions and bone sequestra is lower at MR imaging than at CT (Fig 8). DW imaging may show restricted diffusion due to abscess formation (25); therefore, differentiation of simple osteoradionecrosis from osteoradionecrosis with recurrent tumor may be impossible on the basis of DW imaging findings alone. At PET, osteoradionecrosis can show high FDG uptake due to inflammation, thus yielding false-positive findings of tumor recurrence (Fig 8). In our experience, air inclusions, bone fragmentation, and rim-enhancing lesions with restricted diffusion suggestive of abscess formation are the most reliable imaging signs of osteoradionecrosis. However, because early stages of osteoradionecrosis tend not to involve infection, findings may be equivocal, and differentiation of osteoradionecrosis from early tumor recurrence may be impossible on the basis of a single MR or PET/MR imaging examination. At our institution, whenever we suspect osteoradionecrosis, we perform short-term follow-up imaging because biopsy of irradiated tissues may precipitate further infection and delayed wound healing.

Chondroradionecrosis may develop during radiation therapy or months or up to 30 years later (13,82,83). Imaging features of chondroradionecrosis include intense focal FDG uptake, deep gas-containing ulcerations, gas inclusions in sclerotic and fragmented cartilages, and restricted diffusion due to abscess formation. Chondroradionecrosis may coexist with recurrent tumor in up to 35% of patients (83). Differentiation of simple chondroradionecrosis from chondroradionecrosis with recurrent tumor may be impossible at DW and PET/MR imaging unless follow-up imaging is performed. In our experience, if typical morphologic signs of chondroradionecrosis are seen at MR imaging or CT and there is no soft-tissue mass or restricted diffusion, associated tumor recurrence is unlikely. Follow-up imaging will confirm absence of recurrent disease.

Arteriopathy and Cerebrovascular Complications after Radiation Therapy.—After radiation therapy, progressive thickening of the carotid wall due to intimal proliferation with or without lipid deposits and accelerated arteriosclerosis are commonly seen (84). Transmural necrosis of the vessel wall can lead to pseudoaneurysm formation, which harbors risk for carotid rupture. Carotid rupture can occur as a consequence of radiation therapy alone, or it may be precipitated by soft-tissue necrosis, associated infection, and exposure to saliva (72,73). Stenosis of the carotid arteries is the most common manifestation of radiation therapy–induced arteriopathy in the head and neck. Stenoses are often bilateral and involve a long segment of the vessel wall. They are related to the radiation therapy port. Although many patients are asymptomatic initially, appropriate imaging surveillance is recommended because delayed cerebrovascular consequences are common.

Thin or ruptured, lipid-rich, and hemorrhagic plaques have high inflammatory activity, which manifests as high FDG uptake at imaging (85). Increased FDG uptake seen in carotid plaques (Fig 9) has been shown to be a predictive factor in plaque rupture (86) and ischemic events. High-resolution MR imaging with dedicated angiographic sequences and curved reconstructions accurately depicts vessel wall alterations, plaque morphology, aneurysms, luminal narrowing, and

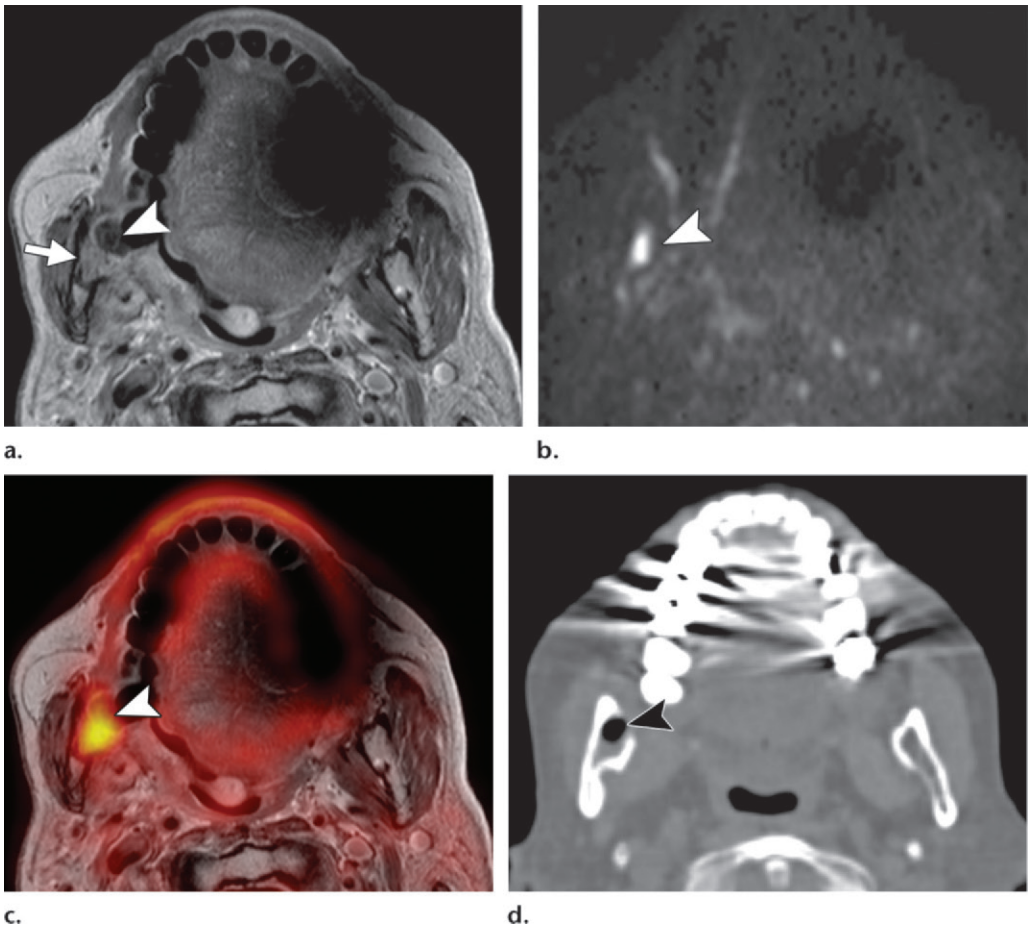

Figure 8. PET/MR imaging findings of mandibular osteoradionecrosis 4 years after radiation therapy for a tonsillar SCC. Axial gadolinium-enhanced T1-weighted MR image **(a)**, DW image (b = 1000 sec/mm^2) **(b)**, fused PET–gadolinium-enhanced T1-weighted MR image **(c)**, and CT image from hybrid PET/CT **(d)** show enhancement of the ascending ramus of the mandible (arrow in **a**), cortical destruction and abscess formation (arrowhead in **a**–**c**), characteristic peripheral rim enhancement, restricted diffusion, and high focal FDG uptake. Restricted diffusion is seen in the abscess, whereas increased FDG uptake is seen in the granulation tissue posterior to the abscess, as expected. Air inclusion (arrowhead in **d**) is better depicted at CT than at MR imaging. Follow-up images obtained 20 months later confirmed findings of benign osteoradionecrosis.

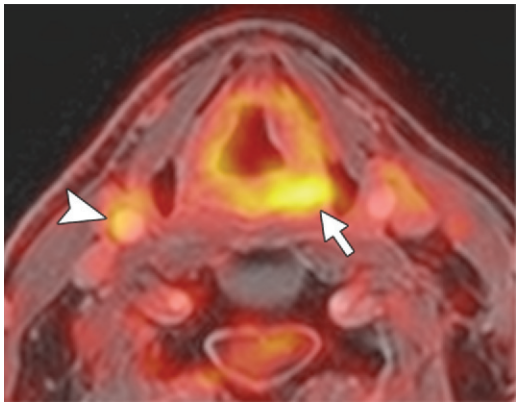

Figure 9. Radiation therapy–induced accelerated arteriosclerosis in a patient with recurrent SCC of the hypopharynx 4 years after radiation therapy and chemotherapy. Fused PET–contrast-enhanced fat-saturated T1-weighted MR image shows FDG uptake in the right common carotid artery wall (arrowhead) due to inflammatory plaques. A small histologically proven recurrent piriform sinus tumor (arrow) has high FDG uptake and demonstrated restricted diffusion at DW imaging (not shown). No metastatic lymph nodes are seen.

cerebrovascular complications. The combined information obtained at PET and MR imaging holds promise to facilitate and complement diagnosis of vulnerable plaques, particularly in patients who have undergone radiation therapy to the head and neck.

Thyroid Disorders.—Radiation therapy is a risk factor for development of hypothyroidism. Hypothyroidism can be seen within the first 6 months after irradiation (87), and its prevalence rises from approximately 20% in the 1st year after radiation therapy to 50% in the 4th year (87). Imaging typically shows progressive thyroid atrophy with decreasing gland width (88) and, in our experience, no restricted diffusion. The relevance of FDG uptake in the thyroid after radiation therapy is still unclear (89); while some authors consider it a common pitfall at PET (66,90), others have suggested that it corresponds to chronic thyroiditis or diffuse thyroid autonomy. Moderate

to intense diffuse FDG uptake in the thyroid after radiation therapy (Fig 10) is generally regarded as benign, but in some cases malignant thyroid lesions may manifest as diffuse FDG uptake (see section on "Incidentalomas") (91).

Radiation Therapy–induced Brain Necrosis.— Radiation therapy ports for tumors in the ethmoid or sphenoid sinus and nasopharynx can include a substantial volume of brain tissue. The deep white matter is typically involved, with relative sparing of the cortex and underlying subcortical arcuate fibers (92). Radiation therapy–induced brain necrosis is irreversible, progressive, and sometimes fatal. It typically occurs within 3 years of radiation therapy (92,93). It can occasionally resolve spontaneously and can result in severe brain atrophy (13).

Imaging findings include increased signal intensity at T2-weighted and fluid-attenuated inversion-recovery (FLAIR) MR imaging (white matter demyelination) and peripheral serpiginous or nodular enhancement after administration of intravenous gadolinium contrast agent (frank necrosis). At DW imaging, radiation therapy–induced brain necrosis manifests as restricted diffusion, given the role of ischemia in the development of this entity. Perfusion studies have limited value in differential diagnosis of recurrent tumor versus radiation therapy necrosis because there is major overlap between relative cerebral blood volume and relative peak height observed in both conditions (93).

FDG PET has limited value in assessment of white matter necrosis because of the inherently high brain glucose metabolism. It has been suggested that delayed imaging performed 3–8 hours after administration of FDG and amino acid PET radiotracers is promising in differentiating recurrent tumors from radiation therapy–induced necrosis. In clinical practice, radiation therapy–induced brain necrosis should be diagnosed by taking into consideration the initial location of the tumor, radiation ports, type and technique of radiation therapy, and time between radiation therapy and imaging (4,93).

Cranial Nerve Palsy.—With the exception of the optic nerve, which is not a true nerve but part of the central nervous system, all cranial nerves are relatively resistant to irradiation; therefore, paralysis is uncommon. The hypoglossal nerve (cranial nerve XII) and recurrent laryngeal nerve (RLN) are the most commonly affected cranial nerves. Early muscle denervation manifests as increased signal intensity on T2-weighted and STIR MR images and muscle enhancement after gadolinium contrast agent administration. Late findings in cranial nerve XII palsy include fatty infiltration of the ipsilateral hemitongue with strict linear demarcation. Muscular atrophy in cranial nerve XII palsy results in tongue deviation toward the healthy contralateral side and posterior bulging of the flaccid paralyzed hemitongue into the oropharynx (94). Late findings in RLN palsy include fatty infiltration of the ipsilateral thyroarytenoid muscle due to atrophy; subsequent enlargement of the ipsilateral ventricle; and piriform sinus and paramedian position of the ipsilateral aryepiglottic fold, false cord, and true vocal cord. PET images in patients with cranial nerve XII or RLN palsy typically show increased FDG uptake in the contralateral healthy muscles due to compensatory hyperactivity, thereby mimicking contralateral tumor recurrence (95). However, coregistered MR images typically show normal contralateral muscle morphology and help avoid this pitfall (Fig 11). When signs of cranial nerve XII or RLN palsy are seen at MR or PET/MR imaging, the entire nerve course must be scrutinized to detect tumor recurrence (94). In the absence of recurrent disease, radiation therapy–induced nerve paralysis should be considered.

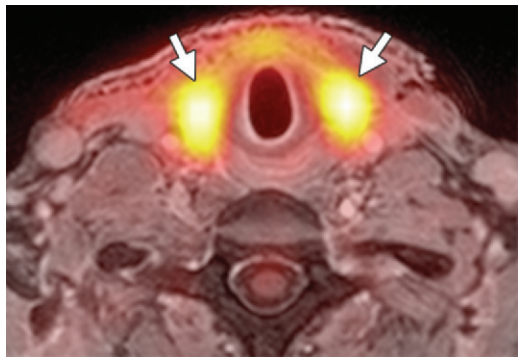

Figure 10. High FDG uptake in the thyroid gland 1 year after radiation therapy in a patient with SCC of the hypopharynx. Fused PET– gadolinium-enhanced fat-saturated T1-weighted MR image shows diffuse, intense, symmetric FDG uptake in the thyroid gland (arrows). Findings at morphologic MR imaging, DW imaging, and thyroid US were normal, as were thyroid test results.

Radiation therapy–induced optic neuropathy is a rare but devastating late effect of radiation therapy for skull base tumors and head and neck SCC of the ethmoid sinuses and nasopharynx (96–98). It most often occurs 10–20 months after treatment and rapidly leads to unilateral or bilateral blindness (96–98). Various theories have been proposed to explain the pathophysiology, such as demyelination, arteriopathy with vascular occlusion, cellular DNA damage, and free radical injury. Predisposing factors include cumulative radiation doses exceeding 50 Gy or single doses exceeding 10 Gy, previous irradiation, and preexisting optic nerve compression by

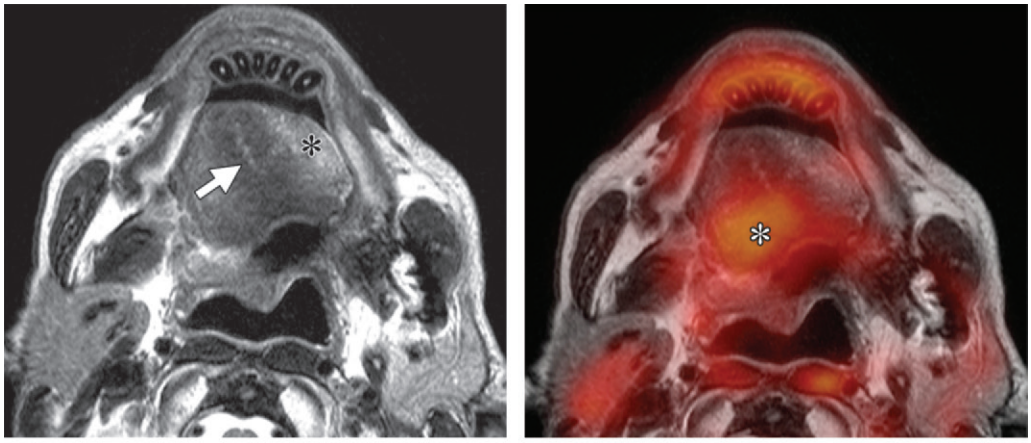

a. b.

Figure 11. PET/MR imaging features of early-stage palsy of left cranial nerve XII in a man who underwent surgery and radiation therapy for oral cavity SCC 3 years earlier. **(a)** Axial T1-weighted MR image shows the deviated tongue septum (arrow) and subtle signs of acute left-tongue denervation (*). **(b)** Fused PET–T1-weighted MR image shows compensatory hyperactivity of the right hemitongue, with increased FDG uptake (*). DW imaging findings were normal (not shown). Findings at follow-up imaging confirmed absence of tumor recurrence and presence of radiation therapy–induced left cranial nerve XII palsy.

the tumor (97). Treatment options are limited, and treatment is often unsuccessful (96–98). MR imaging shows increased signal intensity on T2-weighted and STIR images and variable gadolinium enhancement involving any segment of the optic nerve, optic chiasm, or optic tracts (96–98). The optic nerves may be tortuous with rough-enhancing edges. In long-standing radiation therapy–induced optic neuropathy, MR imaging reveals atrophy of the optic nerve (96–98).

Radiation Therapy–induced Tumors.—The prevalence of radiation therapy–induced tumors in the head and neck is disputed and ranges from 0.04% to 7% (99). They are most often seen in patients who underwent radiation therapy for nasopharyngeal cancer or childhood lymphoma (99). Radiation therapy–induced tumors include SCC, sarcoma, neuroendocrine carcinoma, mucoepidermoid carcinoma, and meningioma (13,99). Typically, these tumors arise in the radiation therapy portal, with a mean delay of 9–13 years between radiation therapy and tumor development (13,99,100). Imaging findings depend on tumor histology and are most often straightforward because of large tumor size (mean reported size, 5 cm) and often extensive bone destruction seen at diagnosis (100). Most radiation therapy–induced tumors show an aggressive destructive pattern and tend to extend into adjacent spaces (100).

Treatment Failure and Recurrent Disease

Treatment failure includes tumor nonsterilization, tumor recurrence, and distant metastases or second primary tumors. Recurrence of head and neck SCC most often manifests clinically during the first 2–3 years after radiation therapy. Because hypertrophic scars, edema, and soft-tissue necrosis also occur during this time interval, differentiation of these entities from recurrent disease is crucial. Currently, there is no consensus regarding use of fat-saturated T2-weighted MR imaging in head and neck oncology. While some authors routinely perform fat-saturated T2-weighted MR imaging (56), others (58,63), ourselves included, prefer T2-weighted MR imaging without fat saturation because high-signal-intensity inflammation and edema can more easily be differentiated from intermediate-signal-intensity tumor and low-signal-intensity scars. Lesion characteristics at DW imaging may further improve diagnostic confidence; recent studies have shown encouraging results with use of DW imaging for detection of recurrent head and neck SCC and differentiation from benign radiation therapy–induced changes (14,15,22,24,31,32,101).

The imaging characteristics of recurrent tumors at DW and PET/MR imaging are similar to those of primary tumors (Fig 12). Recurrent head and neck SCCs are seen as soft-tissue masses with high FDG uptake, moderately high T2 signal intensity, and moderate to high contrast enhancement. At DW imaging, they show restricted diffusion with low ADCs (most often $<1.3 \times 10^{-3}$ mm^2/sec) (14,15,22,24,31,32,101), which allows differentiation from benign radiation therapy–induced changes (ADC $>1.6–1.8 \times 10^{-3}$ mm^2/sec) (15,26,31,32,60,101,102). Although ADCs often allow differentiation between tumor

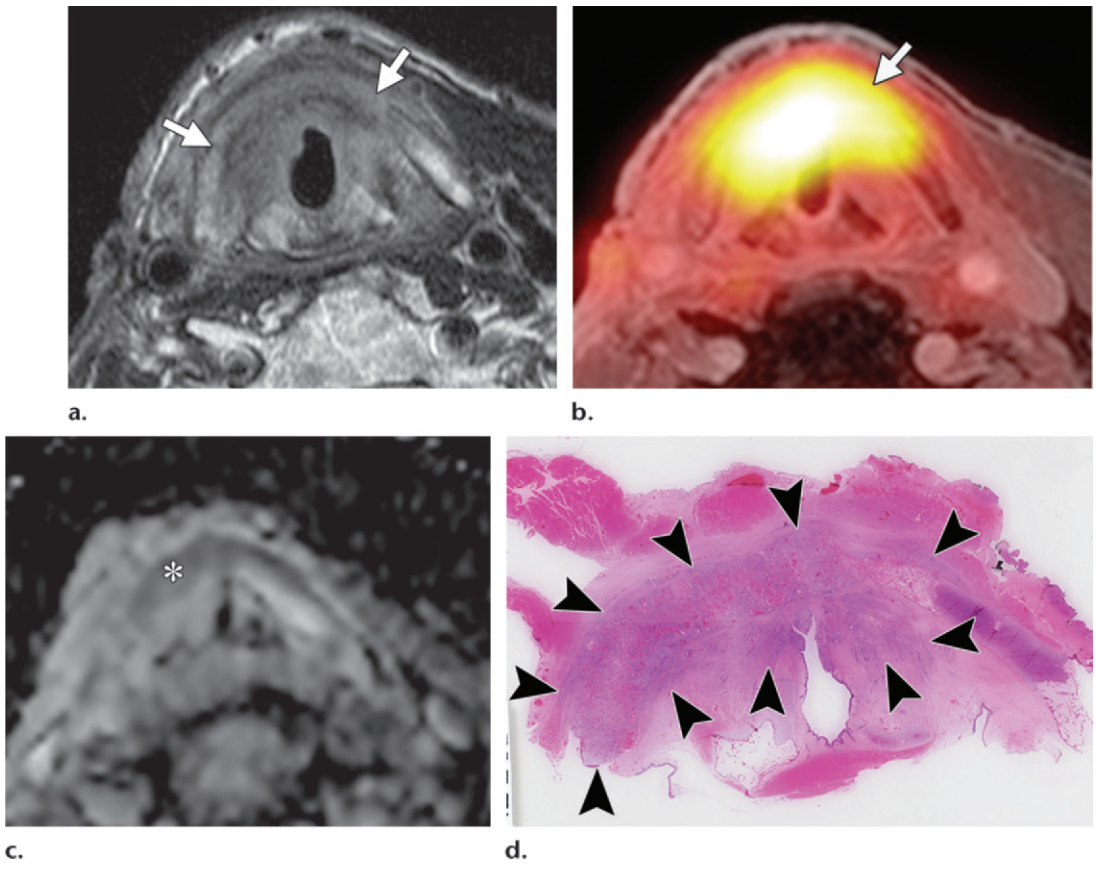

Figure 12. Recurrent SCC of the larynx 2 years after radiation therapy, chemotherapy, and neck dissection in a man with glottic cancer. **(a–c)** Axial T2-weighted MR image **(a)**, fused PET–gadolinium-enhanced fat-saturated T1-weighted MR image **(b)**, and ADC map **(c)** show extensive bilateral tumor recurrence with intermediate signal intensity and tumor invasion of the thyroid cartilage (arrows in **a** and **b**) and prelaryngeal strap muscles. High tumor metabolism (mean SUV, 12) and good tumor conspicuity are shown in **b**. In **c**, restricted diffusion with low ADCs (*) is seen in the thyroid cartilage, but the posterior tumor margins are difficult to assess. **(d)** Photomicrograph from whole-organ histologic section with hematoxylin-eosin stain shows the tumor margins (arrowheads). Histologic analysis showed the right piriform sinus to be equally invaded. There is good concordance between the imaging and histologic findings regarding anterior tumor extension but underestimation of posterolateral tumor spread at imaging, especially at PET and DW imaging.

and inflammation, reported ADC thresholds differ from one series to another because of variable technical parameters used by various investigators (15,26,32, 60). As there may be some overlap between ADCs measured in recurrent tumors and those in radiation therapy–induced inflammatory tissue, DW imaging findings must be correlated with morphologic MR imaging findings. Nevertheless, T1- and T2-weighted images have limited value for precise assessment of deep tumor spread in the irradiated neck, and it has been suggested that morphologic MR imaging may result in underestimation and underclassification of recurrent head and neck SCC (103). As shown in Figure 12, gross tumor volume may also be substantially underestimated on DW and PET images.

Findings of recurrent metastatic lymph nodes at DW and MR imaging are similar to those of metastatic lymph nodes in primary tumors (Fig 1). Characteristic MR imaging findings of nodal metastases from head and neck SCC include rounded shape, increased size (minimum axial diameter >1 cm), absent fatty hilum, inhomogeneous contrast enhancement, nodal necrosis, and occasionally a reticulated aspect of the surrounding fatty tissue that suggests extranodal tumor spread. Although metastatic lymph nodes typically display low ADCs, ADCs can be high because of nodal necrosis, and careful correlation with morphologic images, in particular gadolinium-enhanced fat-saturated T1-weighted MR images, is necessary. Small metastatic lymph nodes (<4 mm) and lymph nodes with micrometastases are below the resolution of currently available morphologic MR and DW images, and some authors have suggested that US-guided fine-needle aspiration biopsy may be superior to PET/CT, CECT, and MR imaging for detection of small metastatic nodes (104,105).

At PET/MR imaging, recurrent tumors and recurrent nodes often display high focal FDG uptake (Figs 1, 12). FDG PET has been shown to have a high negative predictive value (90%–97%)

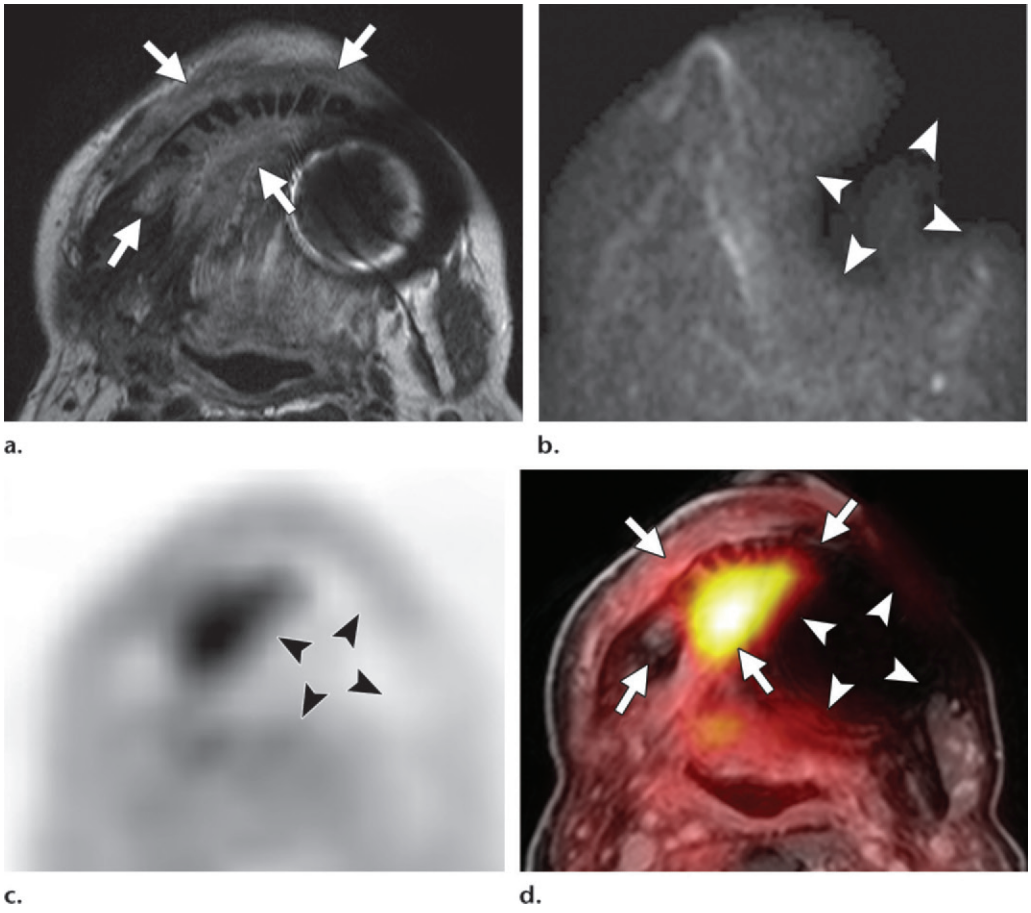

Figure 13. Dental hardware artifact leading to tumor underestimation at follow-up imaging 4 years after radiation therapy in a patient with oral cavity SCC. Axial T2-weighted MR image **(a)**, corresponding axial DW image (b = 1000 sec/mm^2) **(b)**, PET image **(c)**, and fused PET–gadolinium-enhanced fat-saturated T1-weighted MR image **(d)** show an intermediate-signal-intensity recurrent tumor (arrows in **a** and **d**) that invades the mandible. Arrowheads in **b–d** indicate dental hardware artifact. Because of the poor quality of the DW image, the large tumor is not seen in **b**; it also appears smaller in **c** than in **a**. Histologic analysis revealed that tumor size was underestimated on all images and that the lesion equally invaded the left vestibule and left floor of the mouth.

in the posttreatment situation (16,55,106), which allows reliable exclusion of local-regional residual or recurrent disease. Although they are rare, false-negative PET findings can be seen in four situations: *(a)* small tumor size, *(b)* recurrence in areas with inherently high FDG uptake (typically the skull base), *(c)* necrotic tumor, and *(d)* tumor with intrinsically low glucose metabolism. The positive predictive value of PET/CT is moderate (63%–77%), which leads to a considerable number of false-positive findings. Reasons for false-positive FDG PET findings include inflammatory and infectious conditions (see the section on "Pitfalls").

Whole-body PET/MR imaging can depict distant metastases and second primary tumors (16,18,21). Second primary tumors in patients with head and neck SCC recurrence are most often detected in the head and neck area, lungs, or esophagus. Lung metastases may be missed at total body PET/MR imaging (107) unless thin-section high-resolution images are obtained (21). As recently suggested, although conspicuity of lung lesions may be inferior at PET/MR imaging compared with at PET/CT, lung nodules with high FDG uptake are detected equally well with both modalities (18,21).

Pitfalls

Susceptibility Artifacts from Dental Hardware or Osteosynthesis Material

Susceptibility artifacts due to dental hardware or osteosynthesis material (typically after mandibular resection) are commonly seen in the head and neck. They are more pronounced at high field strengths and on DW images (14,27,101). Susceptibility artifacts lead to spatial distortion of surrounding anatomy (especially on DW images), which results in underestimation of tumor size and extension and incorrect tumor localization (Fig 13) (21). In addition, susceptibility artifacts lead to lack of signal intensity on MR imaging–based attenuation correction maps obtained with hybrid PET/MR imaging systems, which results

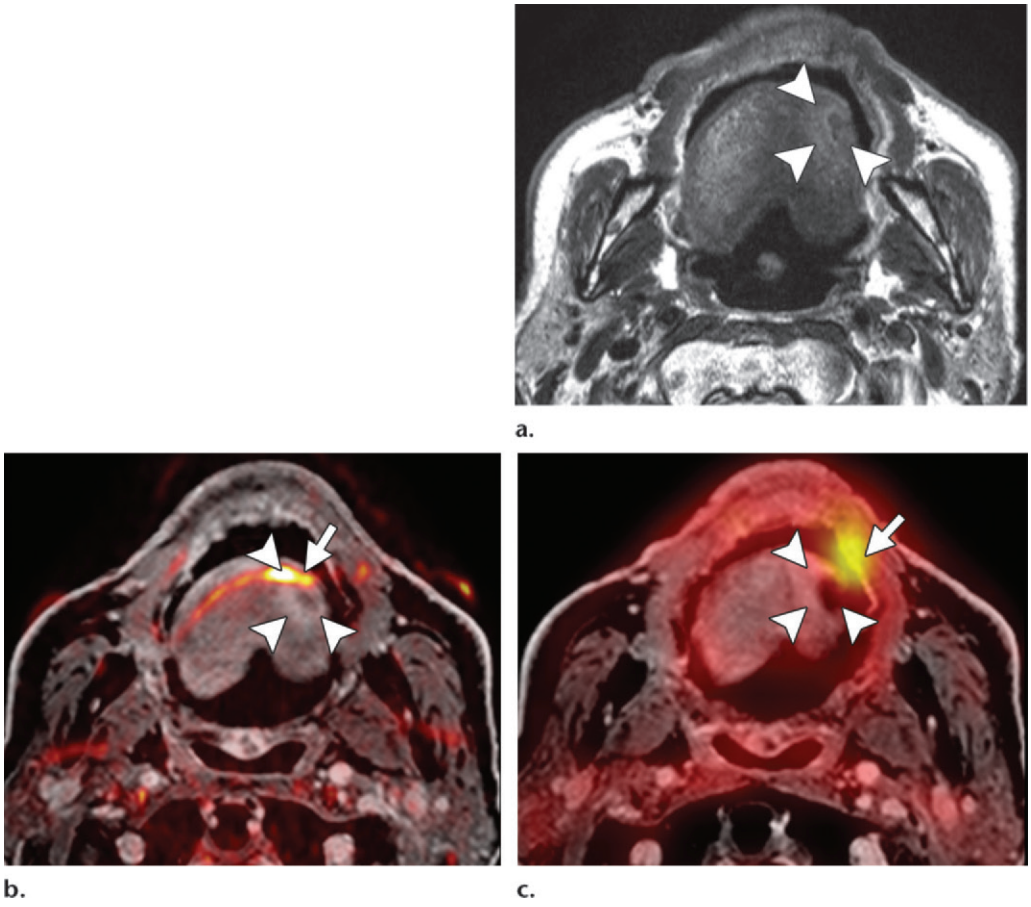

Figure 14. Diffeomorphic miscoregistration between morphologic MR and DW images and anatomic miscoregistration between PET and MR images obtained 2 years after radiation therapy and chemotherapy in a patient with laryngeal SCC. Axial gadolinium-enhanced T1-weighted MR image **(a)**, fused DW (b = 1000 sec/mm^2)–gadolinium-enhanced fat-saturated T1-weighted MR image **(b)**, and fused PET–gadolinium-enhanced fat-saturated T1-weighted MR image **(c)** show a histologically proven second metachronous tumor in the left aspect of the tongue (arrowheads indicate actual tumor size and placement). Because of major geometric distortion in **b**, the tumor appears to be smaller and located anteriorly (arrow in **b**). Because of patient motion in **c**, the tumor appears to be located in the cheek (arrow in **c**).

in underestimation of calculated SUVs (18,21). Artifacts generated by dental implants also affect PET/CT image quality and SUVs measured at PET/CT (108), leading to decreased SUVs in regions with dark streak artifact and increased SUVs in regions with bright streak artifact (108).

Miscoregistration Artifacts

Miscoregistration artifacts (poor data fusion) are caused by geometric distortion and patient motion. Miscoregistration due to geometric distortion is also called *diffeomorphic miscoregistration* (109). It is best appreciated when DW images obtained at b = 1000 sec/mm^2 are fused with standard anatomic MR images (Fig 14). Fusion of geometrically distorted DW images with nondistorted morphologic MR images can lead to incorrect interpretation of tumor localization. Although recognition of this pitfall may be straightforward in larger tumors, it may be trickier in smaller metastatic lymph nodes, especially in the supraclavicular area (21).

Anatomic miscoregistration may be caused by patient motion, variable head rotation or tilting, or respiratory mismatch between acquisition of MR images and PET datasets (Fig 14) (19,21,26). Anatomic miscoregistration can lead to inaccurate tumor localization or misinterpretation of tumor extension (19), particularly if high-resolution morphologic MR images are not correctly analyzed. Anatomic miscoregistration is a problem encountered not only with hybrid PET/MR imaging systems. It can also be seen with currently available PET/CT systems because PET and CT datasets are acquired sequentially. It is also worth mentioning that software fusion of MR imaging and PET data from separate MR imaging and PET/CT imaging units can yield equally poor-quality image fusion, especially in the infrahyoid neck (110).

To reduce misalignment between MR imaging and PET datasets, immobilizing masks or customized support devices can be used during data

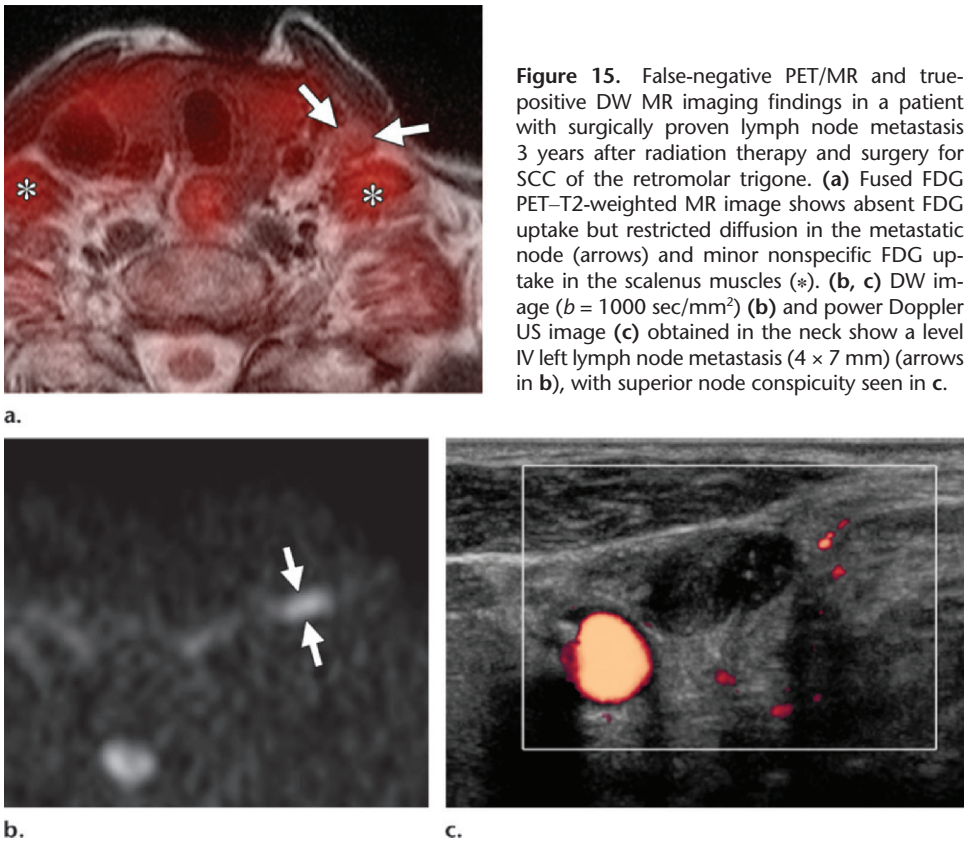

Figure 15. False-negative PET/MR and true-positive DW MR imaging findings in a patient with surgically proven lymph node metastasis 3 years after radiation therapy and surgery for SCC of the retromolar trigone. **(a)** Fused FDG PET–T2-weighted MR image shows absent FDG uptake but restricted diffusion in the metastatic node (arrows) and minor nonspecific FDG uptake in the scalenus muscles (*). **(b, c)** DW image (b = 1000 sec/mm^2) **(b)** and power Doppler US image **(c)** obtained in the neck show a level IV left lymph node metastasis (4 × 7 mm) (arrows in **b**), with superior node conspicuity seen in **c**.

Figure 16. False-negative PET findings due to low glucose metabolism in a patient with recurrent myxoid sarcoma in the maxillary sinus who underwent surgery and radiation therapy 1 year earlier. Fused PET–T2-weighted MR image shows absent FDG uptake in a lesion in the lateral orbital wall (arrows), with high signal intensity due to the myxoid matrix. The lesion showed moderate gadolinium enhancement and no restricted diffusion (not shown). Surgery confirmed sarcoma recurrence.

acquisition, and respiratory mismatch can be corrected with use of respiratory-gated techniques (19,21,111). Current software fusion systems mostly use rigid registration, which consists of mathematically transforming the low-resolution functional image (PET or DW) to match the high-resolution anatomic image (MR) (21,111–115). Although rigid registration may yield good results in nonmoving organs such as the brain, it is less robust in the head and neck. Nonrigid registration algorithms utilize mathematical models that take properties of deformable tissues into consideration (111–115). Deformable image registration methods, such as hyperelastic warping, can be used to obtain motion-corrected PET images based on dynamic MR imaging acquisitions (113). Nevertheless, these new techniques are not yet widely available in clinical practice.

Insufficient Scanner Resolution and Low FDG Avidity

Small tumors may be missed at FDG PET unless intense radiotracer uptake is present because they are below the resolution of current PET scanners. Therefore, false-negative results can occur, especially in metastatic lymph nodes (Fig 15). The often-cited minimum diameter of 8 mm required for detection of metastatic lymph nodes at PET is empirical and probably overestimated, particularly with newer time-of-flight PET systems and improved high-resolution PET reconstructions dedicated to the head and neck (17,116). Therefore, when possible, PET reconstructions in the head and neck should be done using thin 2-mm sections. As previously mentioned, some malignant tumors (well-differentiated sarcomas and necrotic tumors) may not be avid and may cause false-negative results (Fig 16). Lesion prox-

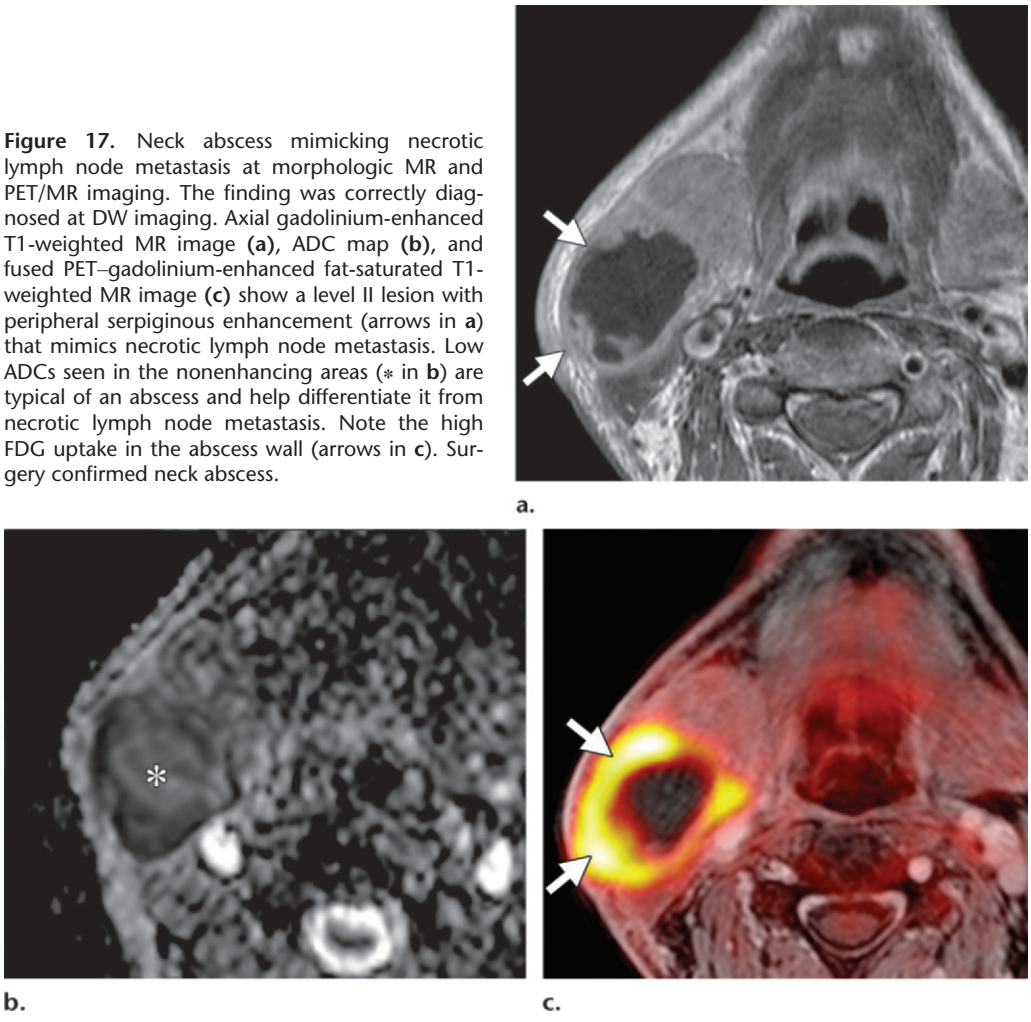

Figure 17. Neck abscess mimicking necrotic lymph node metastasis at morphologic MR and PET/MR imaging. The finding was correctly diagnosed at DW imaging. Axial gadolinium-enhanced T1-weighted MR image **(a)**, ADC map **(b)**, and fused PET–gadolinium-enhanced fat-saturated T1-weighted MR image **(c)** show a level II lesion with peripheral serpiginous enhancement (arrows in **a**) that mimics necrotic lymph node metastasis. Low ADCs seen in the nonenhancing areas (∗ in **b**) are typical of an abscess and help differentiate it from necrotic lymph node metastasis. Note the high FDG uptake in the abscess wall (arrows in **c**). Surgery confirmed neck abscess.

imity to highly metabolic brain tissue may also yield false-negative findings at PET. The complementary information obtained at high-resolution morphologic MR imaging and DW/MR imaging can decrease the number of false-negative findings (Fig 16).

False-Positive Findings Due to Inflammatory and Infectious Diseases

Inflammatory or infectious conditions can lead to false-positive PET findings in the irradiated neck, and correlation with DW imaging findings can help solve the diagnostic dilemma (Fig 17). In clinical practice, no PET/MR imaging examination should be performed without knowledge of clinical findings, especially if an infectious event is suspected. Although analysis of DW imaging findings may be helpful to differentiate tumor necrosis from abscess (Fig 17), US-guided fine-needle aspiration biopsy may still be necessary, especially in patients with necrotic tumors and superimposed secondary infection.

A special problem in patients with recurrent disease and associated peritumoral inflammation is difficulty in precisely delineating tumor margins because tumor and coexisting inflammation may show similar FDG uptake. Analysis of T2 signal intensity and DW images is helpful because peritumoral inflammation often has high T2 signal intensity, high contrast enhancement on T1-weighted MR images, and high ADCs, whereas head and neck SCC displays characteristic intermediate T2 signal intensity, moderate contrast enhancement on T1-weighted MR images, and lower ADCs (31,32,60,101,102).

Iatrogenic focal uptake of FDG caused by recent surgery, tracheostomy cannula, nasogastric tube, biopsy, endosseous implants, or dental extractions is frequent, and PET/MR imaging interpretation is usually straightforward, especially when clinical findings and patient history are known.

Incidentalomas

Incidentalomas are incidental findings seen outside the targeted organ. According to the literature, thyroid incidentalomas are seen in 2.5% of PET studies (91). Most often, thyroid incidentalomas

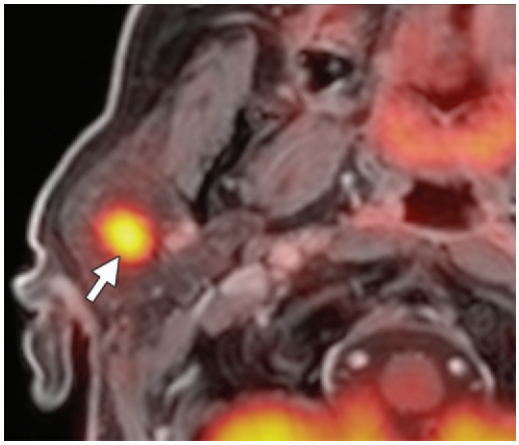

Figure 18. Incidentaloma detected in a woman 4 months after radiation therapy for SCC of the larynx. Fused PET–gadolinium-enhanced fat-saturated T1-weighted MR image shows an intraparotid lesion (arrow) with high FDG uptake (SUV, 10). Additional MR images (not shown) demonstrated well-defined borders, strong homogeneous enhancement, and restricted diffusion. US-guided fine-needle aspiration biopsy confirmed a Warthin tumor.

demonstrate focal uptake; however, in up to 21% of cases, diffuse uptake is seen (91). Most thyroid incidentalomas represent benign thyroid nodules; nevertheless, malignant lesions (mainly papillary and follicular thyroid cancers) can occur in 15%–50% of cases (91,117–119). SUVs do not allow differentiation of benign from malignant thyroid lesions (91), and further evaluation with US-guided fine-needle biopsy is mandatory.

PET/MR imaging of patients with head and neck SCC may depict further incidental abnormalities in the head and neck area, such as Warthin tumors (Fig 18) or lymph nodes with high radiotracer uptake due to coexistent granulomatous diseases. Incidentalomas may also be detected in the rest of the body (120–123). Bladder cancer, breast cancer, benign or malignant adrenal lesions, and mediastinal tuberculosis have been reported (120–123). Incidentalomas require further diagnostic workup. In general, most incidental masses seen at PET/MR imaging are benign. However, because malignant lesions can also occur, in our institution we routinely perform US- or CT-guided biopsy when imaging findings are not pathognomonic for benign disease.

Conclusion

Complementary use of DW and PET/MR imaging may increase diagnostic confidence for differentiating recurrent disease from radiation therapy–induced changes and complications; unnecessary biopsies can potentially be avoided. An overview of imaging findings that allow differentiation of recurrent tumors from radiation therapy–induced complications is provided in Table 3. In this article, we have discussed the added value of DW and PET/MR imaging in evaluation of the irradiated neck, as well as pitfalls related to technical parameters and image interpretation and how to avoid them.

References

1. Lefebvre JL. Laryngeal preservation in head and neck cancer: multidisciplinary approach. Lancet Oncol 2006;7(9):747–755.
2. Argiris A, Karamouzis MV, Raben D, Ferris RL. Head and neck cancer. Lancet 2008;371(9625):1695–1709.
3. Corvò R. Evidence-based radiation oncology in head and neck squamous cell carcinoma. Radiother Oncol 2007;85(1):156–170.
4. Saito N, Nadgir RN, Nakahira M, et al. Posttreatment CT and MR imaging in head and neck cancer: what the radiologist needs to know. RadioGraphics 2012;32(5):1261–1282; discussion 1282–1284.
5. Prescribing, recording, and reporting photon-beam intensity-modulated radiation therapy (IMRT): contents. J ICRU 2010;10(1). doi: 10.1093/jicru/ndq002.
6. Lapeyre M, Toledano I, Bourry N, Bailly C, Cachin F. Target volume delineation for head and neck cancer intensity-modulated radiotherapy [in French]. Cancer Radiother 2011;15(6-7):466–472.
7. Eisbruch A, Foote RL, O'Sullivan B, Beitler JJ, Vikram B. Intensity-modulated radiation therapy for head and neck cancer: emphasis on the selection and delineation of the targets. Semin Radiat Oncol 2002;12(3):238–249.
8. Yao M, Dornfeld KJ, Buatti JM, et al. Intensity-modulated radiation treatment for head-and-neck squamous cell carcinoma: the University of Iowa experience. Int J Radiat Oncol Biol Phys 2005;63(2):410–421.
9. Chao KS, Wippold FJ, Ozyigit G, Tran BN, Dempsey JF. Determination and delineation of nodal target volumes for head-and-neck cancer based on patterns of failure in patients receiving definitive and postoperative IMRT. Int J Radiat Oncol Biol Phys 2002;53(5):1174–1184.
10. Harari PM, Song S, Tomé WA. Emphasizing conformal avoidance versus target definition for IMRT planning in head-and-neck cancer. Int J Radiat Oncol Biol Phys 2010;77(3):950–958.
11. Gorthi S, Duay V, Houhou N, et al. Segmentation of head and neck lymph node regions for radiation therapy planning using active contour-based atlas registration. IEEE J Sel Top Signal Process 2009;3(1):135–147.
12. Stone HB, Coleman CN, Anscher MS, McBride WH. Effects of radiation on normal tissue: consequences and mechanisms. Lancet Oncol 2003;4(9):529–536.
13. Becker M, Schroth G, Zbären P, et al. Long-term changes induced by high-dose irradiation of the head and neck region: imaging findings. RadioGraphics 1997;17(1):5–26.
14. Vandecaveye V, De Keyzer F, Dirix P, Lambrecht M, Nuyts S, Hermans R. Applications of diffusion-weighted magnetic resonance imaging in head and neck squamous cell carcinoma. Neuroradiology 2010;52(9):773–784.
15. Vandecaveye V, De Keyzer F, Nuyts S, et al. Detection of head and neck squamous cell carcinoma with diffusion weighted MRI after (chemo) radiotherapy: correlation between radiologic and histopathologic findings. Int J Radiat Oncol Biol Phys 2007;67(4):960–971.

Table 3: Differentiation of Recurrent Head and Neck SCC from Radiation Therapy–induced Changes and Complications at DW and PET/MR Imaging

Pathologic Condition	Timing of Occurrence after Radiation Therapy	T2-weighted Signal Intensity	T1-weighted Signal Intensity	Contrast Enhancement	Morphology	ADC	FDG Uptake
Scar tissue	Within 2 years	Very low	Very low	Absent in late scar	Triangular or linear, deformation of adjacent tissues	Very low	High in early scar, low in late scar
Soft-tissue necrosis	Within 2 years	Very high	Intermediate to low	Absent	Nonenhancing tissue, mucosal ulceration, fistula formation	High	Variable, depending on presence of granulation tissue
Granulation tissue	Within 2 years	Moderate to high	Intermediate to low	Strong, focal, or poorly defined, with or without soft-tissue necrosis	Diffuse lesion around area of necrosis or diffuse lesion without necrosis	High	High, diffuse, or focal
Osteoradionecrosis and chondronecrosis	4 months–15 years	Mix of low and high signal intensity in marrow spaces	Intermediate to low	Variable, depending on presence of abscess	Bony fragmentation, gas-containing sequestrum with or without rim-enhancing abscess, no soft-tissue mass	Low if abscess, otherwise high	Variable, depending on presence of abscess and degree of infection or inflammation
Recurrent tumor	Within 2–3 years	"Evil gray"	Intermediate to low	Moderate	Mass lesion	Low	High

16. Kwee TC, Takahara T, Ochiai R, et al. Complementary roles of whole-body diffusion-weighted MRI and ^{18}F-FDG PET: the state of the art and potential applications. J Nucl Med 2010;51(10):1549–1558.
17. Torigian DA, Zaidi H, Kwee TC, et al. PET/MR imaging: technical aspects and potential clinical applications. Radiology 2013;267(1):26–44.
18. Varoquaux A, Rager O, Poncet A, et al. Detection and quantification of focal uptake in head and neck tumours: ^{18}F-FDG PET/MR versus PET/CT. Eur J Nucl Med Mol Imaging 2014;41(3):462–475.
19. Vargas MI, Becker M, Garibotto V, et al. Approaches for the optimization of MR protocols in clinical hybrid PET/MRI studies. MAGMA 2013;26(1):57–69.
20. Purohit BS, Dulguerov P, Burkhardt K, Becker M. Dedifferentiated laryngeal chondrosarcoma: combined morphologic and functional imaging with positron-emission tomography/magnetic resonance imaging. Laryngoscope 2014;124(7):E274–E277.
21. Becker M, Zaidi H. Imaging in head and neck squamous cell carcinoma: the potential role of PET/MRI. Br J Radiol 2014;87(1036):20130677.
22. Thoeny HC. Diffusion-weighted MRI in head and neck radiology: applications in oncology. Cancer Imaging 2011;10:209–214.
23. Vandecaveye V, Dirix P, De Keyzer F, et al. Diffusion-weighted magnetic resonance imaging early after chemoradiotherapy to monitor treatment response in head-and-neck squamous cell carcinoma. Int J Radiat Oncol Biol Phys 2012;82(3):1098–1107.
24. King AD, Chow KK, Yu KH, et al. Head and neck squamous cell carcinoma: diagnostic performance of diffusion-weighted MR imaging for the prediction of treatment response. Radiology 2013;266(2):531–538.
25. Koç O, Paksoy Y, Erayman I, Kivrak AS, Arbag H. Role of diffusion weighted MR in the discrimination diagnosis of the cystic and/or necrotic head and neck lesions. Eur J Radiol 2007;62(2):205–213.

26. Varoquaux A, Rager O, Lovblad KO, et al. Functional imaging of head and neck squamous cell carcinoma with diffusion-weighted MRI and FDG PET/CT: quantitative analysis of ADC and SUV. Eur J Nucl Med Mol Imaging 2013;40(6):842–852.
27. Chawla S, Kim S, Wang S, Poptani H. Diffusion-weighted imaging in head and neck cancers. Future Oncol 2009;5(7):959–975.
28. Choi SH, Paeng JC, Sohn CH, et al. Correlation of ^{18}F-FDG uptake with apparent diffusion coefficient ratio measured on standard and high *b* value diffusion MRI in head and neck cancer. J Nucl Med 2011;52(7):1056–1062.
29. Fruehwald-Pallamar J, Czerny C, Mayerhoefer ME, et al. Functional imaging in head and neck squamous cell carcinoma: correlation of PET/CT and diffusion-weighted imaging at 3 Tesla. Eur J Nucl Med Mol Imaging 2011;38(6):1009–1019.
30. Nakajo M, Nakajo M, Kajiya Y, et al. FDG PET/CT and diffusion-weighted imaging of head and neck squamous cell carcinoma: comparison of prognostic significance between primary tumor standardized uptake value and apparent diffusion coefficient. Clin Nucl Med 2012;37(5):475–480.
31. Abdel Razek AA, Kandeel AY, Soliman N, et al. Role of diffusion-weighted echo-planar MR imaging in differentiation of residual or recurrent head and neck tumors and posttreatment changes. AJNR Am J Neuroradiol 2007;28(6):1146–1152.
32. Tshering Vogel DW, Zbaeren P, Geretschlaeger A, Vermathen P, De Keyzer F, Thoeny HC. Diffusion-weighted MR imaging including bi-exponential fitting for the detection of recurrent or residual tumour after (chemo) radiotherapy for laryngeal and hypopharyngeal cancers. Eur Radiol 2013;23(2):562–569.
33. Abgral R, Querellou S, Potard G, et al. Does ^{18}F-FDG PET/CT improve the detection of posttreatment recurrence of head and neck squamous cell carcinoma in patients negative for disease on clinical follow-up? J Nucl Med 2009;50(1):24–29.
34. Hustinx R, Lucignani G. PET/CT in head and neck cancer: an update. Eur J Nucl Med Mol Imaging 2010;37(3):645–651.
35. Quon A, Fischbein NJ, McDougall IR, et al. Clinical role of ^{18}F-FDG PET/CT in the management of squamous cell carcinoma of the head and neck and thyroid carcinoma. J Nucl Med 2007;48(suppl 1):S58–S67.
36. Blodgett TM, Fukui MB, Snyderman CH, et al. Combined PET-CT in the head and neck. I. Physiologic, altered physiologic, and artifactual FDG uptake. RadioGraphics 2005;25(4):897–912.
37. Machtay M, Natwa M, Andrel J, et al. Pretreatment FDG-PET standardized uptake value as a prognostic factor for outcome in head and neck cancer. Head Neck 2009;31(2):195–201.
38. Haerle SK, Huber GF, Hany TF, Ahmad N, Schmid DT. Is there a correlation between ^{18}F-FDG-PET standardized uptake value, T-classification, histological grading and the anatomic subsites in newly diagnosed squamous cell carcinoma of the head and neck? Eur Arch Otorhinolaryngol 2010;267(10):1635–1640.
39. Imsande HM, Davison JM, Truong MT, et al. Use of ^{18}F-FDG PET/CT as a predictive biomarker of outcome in patients with head-and-neck non-squamous cell carcinoma. AJR Am J Roentgenol 2011;197(4):976–980.
40. Higgins KA, Hoang JK, Roach MC, et al. Analysis of pretreatment FDG-PET SUV parameters in head-and-neck cancer: tumor SUV_{mean} has superior prognostic value. Int J Radiat Oncol Biol Phys 2012;82(2):548–553.
41. Wong RJ, Lin DT, Schöder H, et al. Diagnostic and prognostic value of ^{18}F fluorodeoxyglucose positron emission tomography for recurrent head and neck squamous cell carcinoma. J Clin Oncol 2002;20(20):4199–4208.
42. Schöder H, Carlson DL, Kraus DH, et al. 18F-FDG PET/CT for detecting nodal metastases in patients with oral cancer staged N0 by clinical examination and CT/MRI. J Nucl Med 2006;47(5):755–762.
43. Wang CH, Liang JA, Ding HJ, et al. Utility of TL-201 SPECT in clarifying false-positive FDG-PET findings due to osteoradionecrosis in head and neck cancer. Head Neck 2010;32(12):1648–1654.
44. Purohit BS, Ailianou A, Dulguerov N, et al. FDG-PET/CT pitfalls in oncological head and neck imaging. Insights Imaging 2014;5(5):585–602.
45. Zhuang H, Yu JQ, Alavi A. Applications of fluorodeoxyglucose-PET imaging in the detection of infection and inflammation and other benign disorders. Radiol Clin North Am 2005;43(1):121–134.
46. Wiesmüller M, Quick HH, Navalpakkam B, et al. Comparison of lesion detection and quantitation of tracer uptake between PET from a simultaneously acquiring whole-body PET/MR hybrid scanner and PET from PET/CT. Eur J Nucl Med Mol Imaging 2013;40(1):12–21.
47. Arabi H, Rager O, Alem A, Varoquaux A, Becker M, Zaidi H. Clinical assessment of MR-guided 3-class and 4-class attenuation correction in PET/MR. Mol Imaging Biol 2015;17(2):2264-276. doi: 10.1007/s11307-014-0777-5. Published online Aug 6, 2014. Accessed August 14, 2014.
48. Basu S, Zaidi H, Houseni M, et al. Novel quantitative techniques for assessing regional and global function and structure based on modern imaging modalities: implications for normal variation, aging and diseased states. Semin Nucl Med 2007;37(3):223–239.
49. Debnam JM. Imaging of the head and neck following radiation treatment. Pathol Res Int 2011;2011:607820.
50. Moloney EC, Brunner M, Alexander AJ, Clark J. Quantifying fibrosis in head and neck cancer treatment: an overview. Head Neck 37(8):1225–1231. doi:10.1002/hed.23722. Published online July 11, 2014. Accessed August 14, 2014.
51. Hirota S, Tsujino K, Oshitani T, et al. Subcutaneous fibrosis after whole neck irradiation. Int J Radiat Oncol Biol Phys 2002;52(4):937–943.
52. Wratten CR, Poulsen MG, Williamson S, Tripcony L, Keller J, Dickie G. Effect of surgery on normal tissue toxicity in patients treated with accelerated radiotherapy. Acta Oncol 2002;41(1):56–62.
53. Deng J, Ridner SH, Dietrich MS, et al. Prevalence of secondary lymphedema in patients with head and neck cancer. J Pain Symptom Manage 2012;43(2):244–252.
54. Nömayr A, Lell M, Sweeney R, Bautz W, Lukas P. MRI appearance of radiation-induced changes of normal cervical tissues. Eur Radiol 2001;11(9):1807–1817.
55. Krabbe CA, Pruim J, Dijkstra PU, et al. ^{18}F-FDG PET as a routine posttreatment surveillance tool in oral and oropharyngeal squamous cell carcinoma: a prospective study. J Nucl Med 2009;50(12):1940–1947.
56. King AD, Keung CK, Yu KH, et al. T2-weighted MR imaging early after chemoradiotherapy to evaluate treatment response in head and neck squamous cell carcinoma. AJNR Am J Neuroradiol 2013;34(6):1237–1241.
57. Fajardo LF. The pathology of ionizing radiation as defined by morphologic patterns. Acta Oncol 2005;44(1):13–22.
58. Farina D, Borghesi A, Botturi E, Ravanelli M, Maroldi R. Treatment monitoring of paranasal sinus tumors by magnetic resonance imaging. Cancer Imaging 2010;10:183–193.
59. Glazer HS, Niemeyer JH, Balfe DM, et al. Neck neoplasms: MR imaging. II. Posttreatment evaluation. Radiology 1986;160(2):349–354.
60. Sadick M, Schoenberg SO, Hoermann K, Sadick H. Current oncologic concepts and emerging techniques for imaging of head and neck squamous cell cancer. GMS Curr Top Otorhinolaryngol Head Neck Surg 2012;11:Doc08.
61. Lell M, Baum U, Greess H, et al. Head and neck tumors: imaging recurrent tumor and post-therapeutic changes with CT and MRI. Eur J Radiol 2000;33(3):239–247.
62. Mukherji SK, Wolf GT. Evaluation of head and neck squamous cell carcinoma after treatment. AJNR Am J Neuroradiol 2003;24(9):1743–1746.
63. Becker M, Zbären P, Casselman JW, Kohler R, Dulguerov P, Becker CD. Neoplastic invasion of laryngeal cartilage: reassessment of criteria for diagnosis at MR imaging. Radiology 2008;249(2):551–559.
64. Curtin HD. The "evil gray": cancer and cartilage. Radiology 2008;249(2):410–412.
65. Teymoortash A, Simolka N, Schrader C, Tiemann M, Werner JA. Lymphocyte subsets in irradiation-induced sialadenitis of the submandibular gland. Histopathology 2005;47(5):493–500.

66. Shreve PD, Anzai Y, Wahl RL. Pitfalls in oncologic diagnosis with FDG PET imaging: physiologic and benign variants. RadioGraphics 1999;19(1):61–77; quiz 150–151.
67. Liang Y, Bydder M, Yashar CM, et al. Prospective study of functional bone marrow–sparing intensity modulated radiation therapy with concurrent chemotherapy for pelvic malignancies. Int J Radiat Oncol Biol Phys 2013;85(2):406–414.
68. Huang W, Yang Y, Sun Z, Zeng X. Early radiation-induced bone marrow injury: serial MR imaging during initial 4 weeks after irradiation. Acad Radiol 2009;16(6):733–738.
69. Long NM, Smith CS. Causes and imaging features of false positives and false negatives on ^{18}F-PET/CT in oncologic imaging. Insights Imaging 2011;2(6):679–698.
70. Hunter SE, Scher RL. Clinical implications of radionecrosis to the head and neck surgeon. Curr Opin Otolaryngol Head Neck Surg 2003;11(2):103–106.
71. Debnam JM, Garden AS, Ginsberg LE. Benign ulceration as a manifestation of soft tissue radiation necrosis: imaging findings. AJNR Am J Neuroradiol 2008;29(3):558–562.
72. Chen MY, Mai HQ, Sun R, et al. Clinical findings and imaging features of 67 nasopharyngeal carcinoma patients with postradiation nasopharyngeal necrosis. Chin J Cancer 2013;32(10):533–538.
73. Chin SC, Jen YM, Chen CY, Som PM. Necrotic nasopharyngeal mucosa: an ominous MR sign of a carotid artery pseudoaneurysm. AJNR Am J Neuroradiol 2005;26(2):414–416.
74. Hao SP, Chen HC, Wei FC, Chen CY, Yeh AR, Su JL. Systematic management of osteoradionecrosis in the head and neck. Laryngoscope 1999;109(8):1324–1327; discussion 1327–1328.
75. Avril L, Lombardi T, Ailianou A, et al. Radiolucent lesions of the mandible: a pattern-based approach to diagnosis. Insights Imaging 2014;5(1):85–101.
76. Gevorgyan A, Wong K, Poon I, Blanas N, Enepekides DJ, Higgins KM. Osteoradionecrosis of the mandible: a case series at a single institution. J Otolaryngol Head Neck Surg 2013;42(1):46.
77. Teng MS, Futran ND. Osteoradionecrosis of the mandible. Curr Opin Otolaryngol Head Neck Surg 2005;13(4):217–221.
78. Wu LA, Liu HM, Wang CW, Chen YF, Hong RL, Ko JY. Osteoradionecrosis of the upper cervical spine after radiation therapy for head and neck cancer: differentiation from recurrent or metastatic disease with MR imaging. Radiology 2012;264(1):136–145.
79. Bhatia KS, King AD, Paunipagar BK, et al. MRI findings in patients with severe trismus following radiotherapy for nasopharyngeal carcinoma. Eur Radiol 2009;19(11):2586–2593.
80. Alhilali L, Reynolds AR, Fakhran S. Osteoradionecrosis after radiation therapy for head and neck cancer: differentiation from recurrent disease with CT and PET/CT imaging. AJNR Am J Neuroradiol 2014;35(7):1405–1411.
81. Cheung JP, Wei WI, Luk KD. Cervical spine complications after treatment of nasopharyngeal carcinoma. Eur Spine J 2013;22(3):584–592.
82. Hermans R, Pameijer FA, Mancuso AA, Parsons JT, Mendenhall WM. CT findings in chondroradionecrosis of the larynx. AJNR Am J Neuroradiol 1998;19(4):711–718.
83. Zbären P, Caversaccio M, Thoeny HC, Nuyens M, Curschmann J, Stauffer E. Radionecrosis or tumor recurrence after radiation of laryngeal and hypopharyngeal carcinomas. Otolaryngol Head Neck Surg 2006;135(6):838–843.
84. Dorresteijn LD, Kappelle AC, Scholz NM, et al. Increased carotid wall thickening after radiotherapy on the neck. Eur J Cancer 2005;41(7):1026–1030.
85. Lei-xing X, Jing-jing G, Jing-xue N, et al. Combined application of ^{18}F-fluorodeoxyglucose positron emission tomography/computed tomography and magnetic resonance imaging in early diagnosis of vulnerable carotid atherosclerotic plaques. J Int Med Res 2014;42(1):213–223.
86. Rominger A, Saam T, Wolpers S, et al. ^{18}F-FDG PET/CT identifies patients at risk for future vascular events in an otherwise asymptomatic cohort with neoplastic disease. J Nucl Med 2009;50(10):1611–1620.
87. Colevas AD, Read R, Thornhill J, et al. Hypothyroidism incidence after multimodality treatment for stage III and IV squamous cell carcinomas of the head and neck. Int J Radiat Oncol Biol Phys 2001;51(3):599–604.
88. Miller-Thomas MM, Kumar AJ, Sellin RV, Azimpoor S, Ang KK. The shrinking thyroid: how does thyroid size change following radiation therapy for laryngeal cancer? AJNR Am J Neuroradiol 2009;30(3):613–616.
89. Kim SS, Kim SJ, Bae YT, et al. Factors associated with the development of new onset diffuse thyroid F18-fluorodeoxyglucose uptake after treatment of breast cancer in patients without a history of thyroid disease or thyroid dysfunction. Thyroid 2012;22(1):53–58.
90. Abouzied MM, Crawford ES, Nabi HA. ^{18}F-FDG imaging: pitfalls and artifacts. J Nucl Med Technol 2005;33(3):145–155; quiz 162–163.
91. Bonabi S, Schmidt F, Broglie MA, Haile SR, Stoeckli SJ. Thyroid incidentalomas in FDG-PET/CT: prevalence and clinical impact. Eur Arch Otorhinolaryngol 2012;269(12):2555–2560.
92. Jain R, Narang J, Sundgren PM, et al. Treatment induced necrosis versus recurrent/progressing brain tumor: going beyond the boundaries of conventional morphologic imaging. J Neurooncol 2010;100(1):17–29.
93. Shah R, Vattoth S, Jacob R, et al. Radiation necrosis in the brain: imaging features and differentiation from tumor recurrence. RadioGraphics 2012;32(5):1343–1359.
94. Policeni BA, Smoker WR. Pathologic conditions of the lower cranial nerves IX, X, XI, and XII. Neuroimaging Clin N Am 2008;18(2):347–368, xi.
95. Werner MK, Pfannenberg C, Öksüz MO. Nonspecific FDG uptake in the tongue mimicking the primary tumor in a patient with cancer of unknown primary. Clin Imaging 2011;35(5):405–407.
96. Becker M, Masterson K, Delavelle J, Viallon M, Vargas MI, Becker CD. Imaging of the optic nerve. Eur J Radiol 2010;74(2):299–313.
97. Danesh-Meyer HV. Radiation-induced optic neuropathy. J Clin Neurosci 2008;15(2):95–100.
98. Zhao Z, Lan Y, Bai S, et al. Late-onset radiation-induced optic neuropathy after radiotherapy for nasopharyngeal carcinoma. J Clin Neurosci 2013;20(5):702–706.
99. Abrigo JM, King AD, Leung SF, et al. MRI of radiation-induced tumors of the head and neck in post-radiation nasopharyngeal carcinoma. Eur Radiol 2009;19(5):1197–1205.
100. Cai PQ, Wu YP, Li L, et al. CT and MRI of radiation-induced sarcomas of the head and neck following radiotherapy for nasopharyngeal carcinoma. Clin Radiol 2013;68(7):683–689.
101. Thoeny HC, De Keyzer F, King AD. Diffusion-weighted MR imaging in the head and neck. Radiology 2012;263(1):19–32.
102. Hwang I, Choi SH, Kim YJ, et al. Differentiation of recurrent tumor and posttreatment changes in head and neck squamous cell carcinoma: application of high *b*-value diffusion-weighted imaging. AJNR Am J Neuroradiol 2013;34(12):2343–2348.
103. Zbären P, Christe A, Caversaccio MD, Stauffer E, Thoeny HC. Pretherapeutic staging of recurrent laryngeal carcinoma: clinical findings and imaging studies compared with histopathology. Otolaryngol Head Neck Surg 2007;137(3):487–491.
104. Richards PS, Peacock TE. The role of ultrasound in the detection of cervical lymph node metastases in clinically N0 squamous cell carcinoma of the head and neck. Cancer Imaging 2007;7:167–178.
105. van den Brekel MW, Castelijns JA. What the clinician wants to know: surgical perspective and ultrasound for lymph node imaging of the neck. Cancer Imaging 2005;5(Spec No A):S41–S49.
106. Ong SC, Schöder H, Lee NY, et al. Clinical utility of ^{18}F-FDG PET/CT in assessing the neck after concurrent chemoradiotherapy for locoregional advanced head and neck cancer. J Nucl Med 2008;49(4):532–540.
107. Appenzeller P, Mader C, Huellner MW, et al. PET/CT versus body coil PET/MRI: how low can you go? Insights Imaging 2013;4(4):481–490.
108. Park HH, Shin JY, Lee J, et al. A study on the artifacts generated by dental materials in PET/CT image. Conf Proc IEEE Eng Med Biol Soc 2013;2013:2465–2468.
109. Ruthotto L, Kugel H, Olesch J, et al. Diffeomorphic susceptibility artifact correction of diffusion-weighted magnetic resonance images. Phys Med Biol 2012;57(18):5715–5731.

110. Masterson K, Rager O, Kohler R, Wissmeyer M, Ratib O, Becker M. MR/PET image fusion: feasibility and utility in the loco-regional assessment of head and neck cancer. In: Proceedings of the 11th Annual Congress of the Swiss Society of Nuclear Medicine, Lugano, Switzerland, June 3–5, 2010. Nuklearmed-Nucl Med 2010;49(3):A127, SS415.
111. Nehmeh SA, Erdi YE. Respiratory motion in positron emission tomography/computed tomography: a review. Semin Nucl Med 2008;38(3):167–176.
112. Slomka PJ, Baum RP. Multimodality image registration with software: state-of-the-art. Eur J Nucl Med Mol Imaging 2009;36(suppl 1):S44–S55.
113. Ouyang J, Li Q, El Fakhri G. Magnetic resonance-based motion correction for positron emission tomography imaging. Semin Nucl Med 2013;43(1):60–67.
114. Reducindo I, Arce-Santana E, Campos-Delgado DU, Vigueras-Gomez F. Non-rigid multimodal image registration based on local variability measures and optical flow. Conf Proc IEEE Eng Med Biol Soc 2012;2012:1133–1136.
115. Leibfarth S, Mönnich D, Welz S, et al. A strategy for multimodal deformable image registration to integrate PET/MR into radiotherapy treatment planning. Acta Oncol 2013;52(7):1353–1359.
116. Yamamoto Y, Wong TZ, Turkington TG, Hawk TC, Coleman RE. Head and neck cancer: dedicated FDG PET/CT protocol for detection—phantom and initial clinical studies. Radiology 2007;244(1):263–272.
117. Eloy JA, Brett EM, Fatterpekar GM, et al. The significance and management of incidental ^{18}F fluorodeoxyglucose-positron-emission tomography uptake in the thyroid gland in patients with cancer. AJNR Am J Neuroradiol 2009;30(7):1431–1434.
118. Brindle R, Mullan D, Yap BK, Gandhi A. Thyroid incidentalomas discovered on positron emission tomography CT scanning: malignancy rate and significance of standardised uptake values. Eur J Surg Oncol 2014;40(11):1528–1532.
119. Nayan S, Ramakrishna J, Gupta MK. The proportion of malignancy in incidental thyroid lesions on ^{18}F-FDG PET study: a systematic review and meta-analysis. Otolaryngol Head Neck Surg 2014;151(2):190–200.
120. Al-Hakami HA, Makis W, Anand S, et al. Head and neck incidentalomas on positron emission tomographic scanning: ignore or investigate? J Otolaryngol Head Neck Surg 2011;40(5):384–390.
121. Osman MM, Altinyay ME, Abdelmalik AG, Brickman TM, Varvares MA, Nguyen NC. FDG PET/CT incidental diagnosis of a synchronous bladder cancer as a fourth malignancy in a patient with head and neck cancer. Clin Nucl Med 2011;36(6):496–497.
122. Wong KK, Arabi M, Bou-Assaly W, Marzola MC, Rubello D, Gross MD. Evaluation of incidentally discovered adrenal masses with PET and PET/CT. Eur J Radiol 2012;81(3):441–450.
123. Dunne RM, O'Mahony D, Wilson G, McDermott R, O'Keeffe SA. The role of the breast radiologist in evaluation of breast incidentalomas detected on 18-fluorodeoxyglucose positron emission tomography/CT. Br J Radiol 2013;86(1026):20130034. doi:10.1259/bjr.20130034. Published May 14, 2013. Accessed August 14, 2014.